
A RESOLUTION INDEPENDENT NEURAL OPERATOR

Bahador Bahmani*

Hopkins Extreme Materials Institute
Dept. of Civil and Systems Engineering
Johns Hopkins University
Baltimore, USA
bbahman2@jh.edu

Somdatta Goswami

Dept. of Civil and Systems Engineering
Johns Hopkins University
Baltimore, USA
sgoswam4@jh.edu

Ioannis G. Kevrekidis

Dept. of Chemical and Biomolecular Engineering
Dept. of Applied Mathematics and Statistics
Johns Hopkins University
Baltimore, USA
yannisk@jh.edu

Michael D. Shields

Dept. of Civil and Systems Engineering
Johns Hopkins University
Baltimore, USA
michael.shields@jh.edu

September 24, 2024

ABSTRACT

The Deep operator network (DeepONet) is a powerful yet simple neural operator architecture that utilizes two deep neural networks to learn mappings between infinite-dimensional function spaces. This architecture is highly flexible, allowing the evaluation of the solution field at any location within the desired domain. However, it imposes a strict constraint on the input space, requiring all input functions to be discretized at the same locations; this limits its practical applications. In this work, we introduce a **Resolution Independent Neural Operator (RINO)** that provides a framework to make DeepONet resolution-independent, enabling it to handle input functions that are arbitrarily, but sufficiently finely, discretized. To this end, we propose two dictionary learning algorithms to adaptively learn a set of appropriate continuous basis functions, parameterized as implicit neural representations (INRs), from correlated signals defined on arbitrary point cloud data. These basis functions are then used to project arbitrary input function data as a point cloud onto an embedding space (i.e., a vector space of finite dimensions) with dimensionality equal to the dictionary size, which can be directly used by DeepONet without any architectural changes. In particular, we utilize sinusoidal representation networks (SIRENs) as trainable INR basis functions. The introduced dictionary learning algorithms can be used in a similar way to learn an appropriate dictionary of basis functions for the output function data. This approach can be seen as an extension of POD-DeepONet for cases where the realizations of the output functions have different discretizations, making the Proper Orthogonal Decomposition (POD) approach inapplicable. We demonstrate the robustness and applicability of RINO in handling arbitrarily (but sufficiently richly) sampled input and output functions during both training and inference through several numerical examples.

Keywords Point-Cloud Data · Dictionary Learning · Implicit Neural Representation · Deep Operator Network (DeepONet) · Neural Operator · Scientific Machine Learning

1 Introduction

Partial Differential Equations (PDEs) serve as fundamental mathematical models for a vast array of phenomena in science and engineering. Solving a PDE amounts to computing the underlying solution operator, which maps given input functions such as initial and boundary conditions, source terms, coefficients, etc. to the solution. With the advent

*Corresponding author.

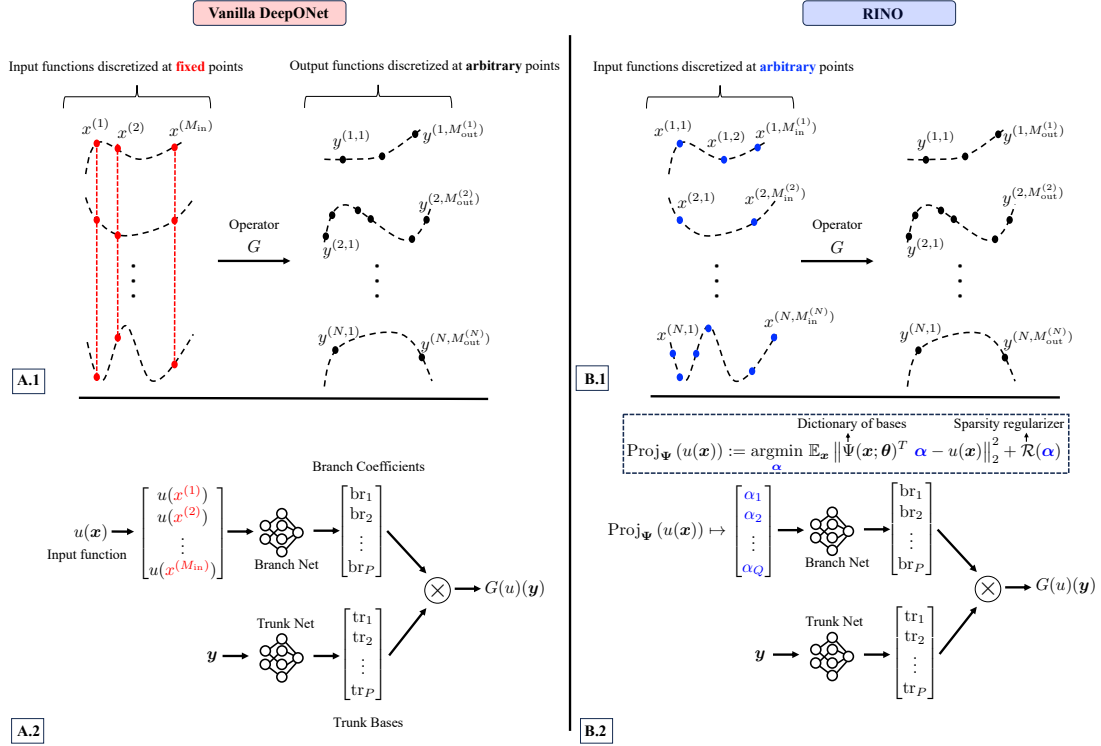


Figure 1: Vanilla DeepONet and RINO in a nutshell. Vanilla DeepONet requires input functions to be sampled at a fixed set of points (A.1), while RINO allows for arbitrary discretization of the input functions (B.1). The branch network in Vanilla DeepONet operates directly on the discretized input functions (A.2), whereas in RINO, the DeepONet operates on the embeddings obtained from projecting the input signal onto a dictionary learned *a priori* (B.2).

of modern machine learning models, new methodologies have emerged for creating fast data-driven emulators to solve parametric PDEs. Since operators are crucial in the context of PDEs, machine learning (ML) architectures that are designed to learn these operators and map functions to functions are increasingly viewed as a suitable paradigm for applying ML techniques to PDEs.

Modern operator learning frameworks employing deep neural networks (DNNs) have emerged as a powerful method for constructing discretization-independent emulators for PDEs that describe physical systems. Neural operators, first introduced in 2019 with the deep operator network (DeepONet) [22], utilize two DNNs to create a surrogate model, enabling fast inference and high generalization accuracy. In this architecture one DNN, known as the branch network, encodes the input functions at fixed sensor points (see Figure 1), while another DNN, the trunk network, encodes information related to the output function at various spatiotemporal coordinates. The solution operator is defined as a linear combination of basis functions learned by the trunk network, with their coefficients learned by the branch network. The design of DeepONet is inspired by the universal approximation theorem for operators proposed by Chen & Chen [9]. The generalized theorem for DeepONet essentially replaces shallow networks used for the branch and trunk net in [9] with DNNs to gain expressivity. Since its introduction, DeepONet has been employed to address challenging problems involving complex high-dimensional dynamical systems [11, 5, 17, 39, 7]. The framework is highly versatile, allowing the two DNNs to adopt various architectures such as convolutional neural networks (CNNs) or multilayer perceptrons (MLPs), depending on the specific problem requirements.

Despite its significant success, a notable limitation of the vanilla DeepONet framework is the need to discretize all input functions in the training and test sets at fixed sensor locations. This requirement can be a major bottleneck in some applications, either in cases where different computational meshes are used or where a single computational mesh is adaptively refined in time or space. In this work, we develop efficient strategies for creating unique continuous representations of input functions without constraints on their discretization, such as the number and location of sensors in the input space of both the labeled training dataset and the testing samples as shown in Figure 1, that can be consistently parameterized and applied directly to existing DeepONet architectures. This results in the new Resolution

Independent Neural Operator (RINO) variant of DeepONet. Note, however, that although they do not require fixed sensor locations, these strategies of course require sufficient resolution to capture the characteristic length or time scales of the underlying function. For example, discretization must still satisfy the classical restriction on the minimal sampling rate due to the Nyquist–Shannon sampling theorem [34].

To achieve discretization independence, we develop a data-driven algorithm that maps an arbitrarily discretized input function realization to its corresponding embedding coordinates. We construct this embedding space by projecting these input function realizations onto a set of fixed, continuous, and fully differentiable basis functions shared across all realizations, where the projection coefficients serve as the embedding coordinates. For flexibility, these basis functions are parameterized by neural networks and are learnable, although they do not have to be and could, for example, be specified *a priori*. Specifically, our algorithm discovers appropriate neural network basis functions from a collection of correlated signals, e.g., input function realizations. This algorithm extends standard dictionary learning techniques from finite-dimensional vector spaces to function spaces. Dictionary learning is an unsupervised machine learning method that identifies a set of basis vectors to represent data as a sparse combination of these basis vectors. It has various applications, including sparse coding [29], image denoising [24], and face recognition [46]. Unlike some classical ML methods such as principal component analysis (PCA), dictionary learning can learn overcomplete basis sets, where the number of basis vectors exceeds the dimensionality of the input space. This may provide more flexibility for signal modeling and representation.

Here, the dictionary construction is performed in an *offline* manner. At the construction stage, we iteratively add new trainable basis functions (i.e., atoms) and their corresponding coefficients (i.e., codes) to reduce the expected residual of the signal reconstruction error across all realizations. Similar to other standard dictionary learning algorithms, we additionally promote the learning towards per-realization sparse coefficients. Once the dictionary is learned, we apply it to unseen cases by reusing the dictionary and solving only for the basis coefficients of the queried realization *online*. This is achieved by projecting the queried signal onto the learned dictionary atoms.

We leverage recent advances in *implicit neural representations (INRs)* [25, 36] to model the dictionary basis functions. These representations are continuous, differentiable functions implicitly defined and parameterized by MLPs. Instead of the *explicit* parameterization of the signal of interest, where the discrete signal values are the parameters (for example, signal values at 2D grids, voxels, point clouds, and meshes), INRs represent the signal values *implicitly* (or indirectly) as a function parameterized by a neural network. This network $\Phi : \mathbf{x} \rightarrow \Phi(\mathbf{x})$ maps spatiotemporal coordinates $\mathbf{x} \in \mathbb{R}^M$ from an M -dimensional space to their corresponding N -dimensional signal values, $\Phi(\mathbf{x}) \in \mathbb{R}^N$. INRs find extensive applications in tasks such as image generation, super-resolution, object reconstruction, and modeling complex signals [36, 37]. INRs offer several advantages. First, the functions are defined on the continuous domain of \mathbf{x} rather than on a discrete grid, enabling the representation to adapt flexibly to various resolutions. Second, they ensure that the function is fully continuous and differentiable with respect to \mathbf{x} , facilitating the use of automatic differentiation, which is crucial for problems requiring access to the function’s gradient. Lastly, they have shown greater memory efficiency compared to grid-based representations [25], as their capacity to model fine details depends on the architecture of the model rather than the grid resolution. The application of INRs as basis functions in RINO is motivated by their resolution invariance, ability to capture fine details, and differentiability. In particular, we utilize sinusoidal representation networks (SIRENs).

Connection with ReNO: The problem of interest in our study is to establish a neural operator learning method that can operate with data sampled irregularly from one realization to another while maintaining relatively consistent accuracy, particularly from the input function perspective. We assume that the function realizations are bandwidth-limited signals and that the density of sensor locations is sufficiently fine, exceeding the minimal Nyquist-Shannon sampling rate. Therefore, we do not explore potential aliasing issues related to sampling below the Nyquist-Shannon rate during training. Representation equivalent Neural Operators (ReNO) [3] were developed to investigate aliasing issues in the context of operator learning and proposes a general formalism based on *frame theory* to determine the conditions under which a discrete representation of an operator is equivalent to its continuous version. Since our dictionary learning algorithm identifies basis functions that are (weakly) orthogonal, they may form a *frame*; Bartolucci et al. [3] show that orthogonality is a sufficient condition for defining a frame. The connection between discrete and continuous representations is established by these frames (basis functions) via the *synthesis operator* (reconstruction operator) and its adjoint, known as the *analysis operator* (projection operator). Therefore, the RINO framework aligns with their frame theory, but the proposed RINO further provides an algorithm to adaptively construct appropriate basis functions (frames) to enable consistent mapping between discrete and continuous representations of signals of interest.

The paper is organized as follows. In Section 2, we describe the components of our proposed framework, namely the operator learning architecture, the concept of learning a dictionary of basis functions, and the parametrization approach via the INRs. In Section 3, we present four numerical examples to test the RINO framework. For each numerical example, we conducted a comprehensive study by varying the input function, the number of sensors, and their

locations. Details about the data generation process are provided in each respective example. Finally, we summarize our observations and provide concluding remarks in Section 4. An important discussion on the connection between our proposed function-space dictionary learning algorithm and classical Gappy POD (GPOD), as well as alternative possibilities using random projections to achieve vector representations of input or output function data, is presented in Appendix F.

2 Formulation

In Section 2.1, we revisit the operator learning problem statement that is the focus of this work. We utilize the DeepONet formalism to learn operators in a data-driven manner and develop a formulation that accepts a resolution-independent embedding of the input functions (e.g., spatially and/or temporally dependent source terms, initial conditions, material properties, etc.) instead of directly working with input function data in the original space. This approach eliminates the resolution dependency of the vanilla DeepONet from the perspective of the input function. At the end of this section, we present an operator learning formulation that bypasses the need for an unknown trunk during the operator learning training. This formulation extends the POD-DeepONet approach into a fully resolution-independent framework. Then, in Section 2.2, we introduce two algorithms to learn appropriate parametrized basis functions to represent input or output function data in a resolution-independent manner. Finally, in Section 2.3, we specifically introduce the parametrization of our basis functions as INRs.

2.1 Operator Learning Between Function Spaces

Let \mathcal{U} and \mathcal{S} be Banach spaces of vector-valued functions, as follows:

$$\mathcal{U} = \{u : \mathcal{X} \rightarrow \mathbb{R}^{d_u}\}, \quad \mathcal{X} \subseteq \mathbb{R}^{d_x} \quad (1)$$

$$\mathcal{S} = \{s : \mathcal{Y} \rightarrow \mathbb{R}^{d_s}\}, \quad \mathcal{Y} \subseteq \mathbb{R}^{d_y}. \quad (2)$$

where \mathcal{U} and \mathcal{S} denote the *input functions* and *output functions*, respectively for the operator learning problem. Assuming there is a ground-truth operator $\mathcal{G} : \mathcal{U} \rightarrow \mathcal{S}$, the operator learning task is to approximate \mathcal{G} with a parameterized functional $\mathcal{F}_\theta : \mathcal{U} \times \Theta \mapsto \mathcal{S}$ where $\Theta \subseteq \mathbb{R}^{\dim(\theta)}$ is the parameter space. The optimal parameters can be found, in the empirical risk minimization sense, as follows:

$$\operatorname{argmin}_{\theta} \mathbb{E}_{u \sim \mu_u} \|\mathcal{G}(u) - \mathcal{F}_\theta(u)\|_{\mathcal{S}}^2 \approx \frac{1}{N} \sum_{i=1}^N \left\| s^{(i)} - \mathcal{F}_\theta(u^{(i)}) \right\|_{\mathcal{S}}^2, \quad (3)$$

where the dataset $\mathcal{D}_{\text{OL}} = \{(u^{(i)}, s^{(i)})\}_{i=1}^N$ contains N pairs of input and output functions with $u^{(i)} \sim \mu_u$ are i.i.d (independent and identically distributed) samples from a probability measure μ_u supported on \mathcal{U} and $s^{(i)} = \mathcal{G}(u^{(i)})$.

In practice, we only have access to finite-dimensional observations of input-output functions, which correspond to their discretized versions. Thus, in the most general setting, the i -th input function $u^{(i)}(x)$ is arbitrarily discretized at $M_{\text{in}}^{(i)}$ input sensor locations and stored as the point cloud $\mathcal{D}_u^{(i)} = \{x^{(i,j)}, \bar{u}^{(i,j)}\}_{j=1}^{M_{\text{in}}^{(i)}}$, where $x^{(i,j)} \in \mathcal{X}$ and $\bar{u}^{(i,j)}(x^{(i,j)}) \in \mathcal{U}$. Similarly, its corresponding output function $s^{(i)}(y)$ is arbitrarily discretized at $M_{\text{out}}^{(i)}$ output sensor locations and stored as a point cloud $\mathcal{D}_s^{(i)} = \{y^{(i,j)}, \bar{s}^{(i,j)}\}_{j=1}^{M_{\text{out}}^{(i)}}$, where $y^{(i,j)} \in \mathcal{Y}$ and $\bar{s}^{(i,j)}(y^{(i,j)}) \in \mathcal{S}$. This general data configuration is schematically illustrated in Figure 1(B.1).

Remark 2.1. In this manuscript, superscript indices are used to denote data-related information. Specifically, a single superscript $(\cdot^{(i)})$ indicates the i -th function realization, which can represent a sample. A double superscript $(\cdot^{(i,j)})$ is used to indicate the j -th observation point (or sensor) within the i -th function realization. For example, $u^{(i)}$ denotes the i -th realization of the function u , and $x^{(i,j)}$ denotes the j -th observation point in the i -th function realization. We use the bar notation \bar{u} to represent the discretized form of the continuous field u , which may include measurement and/or discretization errors.

Various approaches have been developed to approximate the ground truth operator \mathcal{G} using parameterized functions, with neural networks being particularly notable. Two prominent methods are DeepONet and Fourier Neural Operator (FNO) introduced by [22] and [21], respectively. The FNO leverages Fourier transforms to efficiently learn operators on grids, though it can be computationally intensive due to the need for these Fourier transforms. In contrast, DeepONet offers greater architectural flexibility, making it particularly suitable for operations on point cloud data. Within

the DeepONet framework, the parameterized functional $\mathcal{F}_\theta(u)(y)$ has the following structure:

$$\mathcal{G}(u)(y) \approx \mathcal{F}_\theta(u)(y) \stackrel{\text{DeepONet}}{=} \mathcal{F}_\theta^{\text{br}T}(\bar{u}) \mathcal{F}_\theta^{\text{tr}}(y) = \sum_{k=1}^P \text{br}_k(\bar{u}; \theta) \text{tr}_k(y; \theta), \quad (4)$$

where $\mathcal{F}_\theta^{\text{tr}}$ and $\mathcal{F}_\theta^{\text{br}}$ are parameterized functions modeled by suitable neural networks, referred to as the *trunk* and *branch* nets, respectively. The trunk net defines a set of basis functions over the domain of the output function, while the branch net defines the corresponding coefficients, which depend on the input function u . Within this formalism, a finite-dimensional vector representation (i.e., embedding) of the *input function* u is necessary for use in standard neural network architectures. Indeed, the observed data \bar{u} can serve as an effective representation of the input function, as used in the original DeepONet. However, this requires that the input sensor locations remain consistent across all input data, as illustrated in Figure 1(A). This has two drawbacks: first, it makes the resulting approximate operator dependent on the resolution, and second, it may cause the number of parameters in the branch network to become unnecessarily large (and therefore expensive to train), depending on how finely the input functions are discretized.

One approach to mitigate this issue is to find a vector representation of the input data that is resolution-independent. If such a representation exists, we hypothesize that the classical DeepONet can be formulated in this embedding space as follows:

$$\mathcal{G}(u)(y) \approx \sum_{k=1}^P \text{br}_k(\alpha(u); \theta) \text{tr}_k(y; \theta), \quad (5)$$

where $\alpha \in \mathbb{R}^Q$ is an embedding of the input function $u(x)$ in a well-defined embedding space; see Figure 1(B.2) for a schematic of the architecture and Figure 2 for a schematic of the function space mappings. Note that the selection of the embedding can be defined arbitrarily by projecting the input onto a set of continuous orthogonal basis functions (e.g. orthogonal polynomials). However, we aim to identify an optimally compact basis that both improves accuracy and reduces the number of necessary parameters in the operator. In the next section, we will introduce a method to find this desired representation.

The resulting optimization statement for the operator learning task with this embedding, in the discrete sense, solved in this work is as follows:

$$\underset{\theta}{\text{argmin}} \mathbb{E}_i \mathbb{E}_{(y,s) \sim \mathcal{D}_s^{(i)}} \left\| s - \mathcal{F}_\theta(\alpha^{(i)})(y) \right\|_2^2. \quad (6)$$

Remark 2.2. In this paper, the symbol θ is used to represent neural network parameters. Its specific meaning may vary by section, and it denotes the parameters of different functions or models. Readers should refer to the context within each section for the precise definition.

2.1.1 Operator Learning with Predefined Trunk

In the vanilla DeepONet, the trunk network essentially tries to find appropriate basis functions that approximate the output functions. So, if a suitable set of bases already exists for the output function data, it can be directly used. Using this intuition, Lu et al. [23] propose the POD-DeepONet, where the trunk network is replaced by fixed, predefined Proper Orthogonal Decomposition (POD) modes associated with the output functions, resulting in only the branch network being trainable. This approach may facilitate training and improve the accuracy of the operator learning task. However, due to the use of POD, which works on fixed grids, similar discretization dependence issues arise, as with the input function process in the vanilla DeepONet. For example, if the discretization of output functions varies from realization to realization, POD cannot be directly used.

In RINO, we develop dictionary learning algorithms that adaptively learn basis functions for approximating signals defined on arbitrary point clouds. This allows us to project arbitrary signals onto these basis functions and use their corresponding coefficients as appropriate representations in the embedding space. This is the nature of the embedding of the input function in Eq. (5). If such a method exists (as discussed in the next section), it can also be applied *separately* to the output function data. This process would build an appropriate dictionary of basis functions for the output data, which can subsequently be used in the operator learning task as a fixed, predefined trunk (analogous to the POD) as showed in Figure 2(b).

For now, let us additionally assume that the output dictionary $\Psi_S(y) = \{\psi_l^S(y)\}_{l=1}^P$ is known and available for use where $P = |\Psi_S|$. The availability of the input dictionary, denoted by $\Psi_U(x) = \{\psi_l^U(x)\}_{l=1}^Q$ where $Q = |\Psi_U|$, was already assumed in the previous section. Under this setup, which is schematically shown in Figure 2(b), the objective

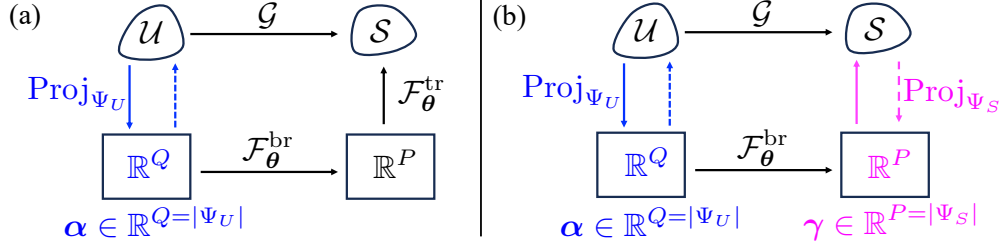


Figure 2: Operator learning with RINO for (a) unknown trunk and (b) predefined trunk basis functions. In (a), only the input functions are embedded using a learned set of basis function and the operator is learned between the embedding space and the output directly by training both branch ($\mathcal{F}_\theta^{\text{br}}$) and trunk ($\mathcal{F}_\theta^{\text{tr}}$) networks. In (b), is functions are learned separately for both output and input function data. Consequently, the operator learning task effectively becomes a mapping between these two constructed subspaces via the branch network $\mathcal{F}_\theta^{\text{br}}$.

function for operator learning is defined as:

$$\arg\min_{\theta} \mathbb{E}_i \mathbb{E}_{(y,s) \sim \mathcal{D}_s^{(i)}} \underbrace{\left\| s - \text{Recon}_{\Psi_S} \left(y; \bar{\gamma}_\theta^{(i)} \right) \right\|_2^2}_{\text{prediction loss}} + \tau \underbrace{\left\| \gamma^{(i)} - \bar{\gamma}_\theta^{(i)} \right\|_2^2}_{\text{embedding consistency loss}}, \quad (7)$$

where $\bar{\gamma}_\theta^{(i)} = \mathcal{F}_\theta^{\text{br}}(\alpha^{(i)})$, $\gamma^{(i)} = \text{Proj}_{\Psi_S}(\mathcal{D}_s^{(i)})$, $\alpha^{(i)} = \text{Proj}_{\Psi_U}(\mathcal{D}_u^{(i)})$, and τ is a penalty factor that controls the extent to which the second term is enforced. The first term in this objective function corresponds to the prediction part of the operator network, while the second term helps the branch network produce a representation consistent with the coefficients of the output basis functions. The reconstruction operator for a dictionary Ψ is defined as follows:

$$\text{Recon}_{\Psi}(\cdot; \gamma) \triangleq \sum_{l=1}^{|\Psi|} \psi_l(\cdot) \gamma_l. \quad (8)$$

The dictionary projection operator will be specified in the next section.

2.2 Dictionary Learning

In this section, we introduce two dictionary learning algorithms to identify a set of basis functions parameterized by neural networks, which are used to approximate signals defined on point cloud data. The first algorithm aims to adaptively find basis functions that capture the *expected* value of the residual across batches of signal realizations, while the second algorithm aims to find a basis each time that is needed to approximate only one realization at a time.

2.2.1 Batch-wise Learning

Given a collection of N signals $U \in \mathbb{R}^{N \times M}$, which are discretized at M locations and assumed to be correlated and share a common structure, the classical dictionary learning goal is to learn a set of Q basis vectors (or *atoms*), $\Psi \in \mathbb{R}^{Q \times M}$, such that all signals in the set can be sufficiently approximated using a sparse linear combination of these basis vectors (see top of Figure 3). A classical example of dictionary learning is PCA, where the goal is to approximate high-dimensional, correlated signals using a few principal components, which serve as basis vectors. Here, we go beyond discovering dictionaries that exist in finite-dimensional vector spaces and instead focus on finding those that reside in continuous function spaces, making them suitable for processing signals defined on irregular domains such as point clouds (see bottom of Figure 3).

Our goal here is to learn a dictionary that can represent the input function $u(x)$; however, the same procedure can be applied to the output function as well. In a general setup, we are given a dataset of N recorded signals, denoted by $\mathcal{D}_u = \{\mathcal{D}_u^{(i)}\}_{i=1}^N$, where each element $\mathcal{D}_u^{(i)}$ contains an arbitrarily discretized version of the i -th function realization $u^{(i)}$, as described in the previous section and depicted in the bottom of Figure 3. If the number and locations of sensors (discretization points) are identical for all signals, the data setup resembles the classical PCA setup.

We aim to find a common set of Q basis functions $\Psi(x) = \{\psi_l(x)\}_{l=1}^Q \equiv [\psi_1(x), \dots, \psi_Q(x)]^T$, *continuously* defined over the domain of u , such that the signal realizations can be represented sufficiently well by a linear combination of

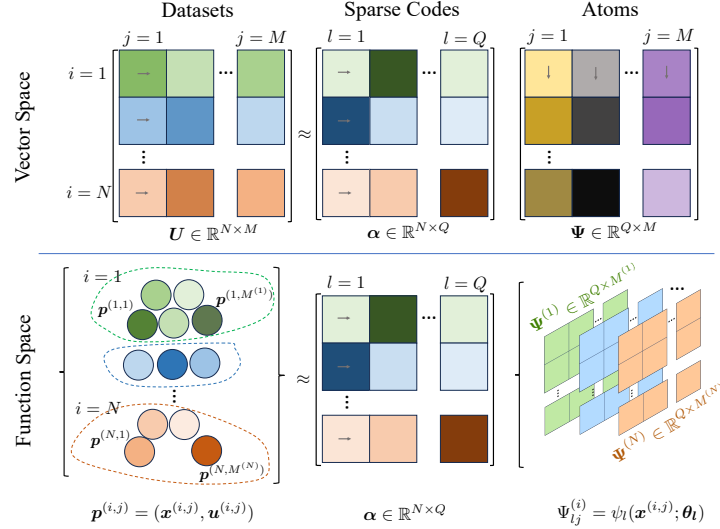


Figure 3: Dictionary learning (**top**) in the classical vector space setup and (**bottom**) in our proposed function space setup. Our method can be directly applied to point cloud signals that are sampled arbitrarily (but sufficiently richly) in terms of the number and location of discretized points. In our method, classical discrete atoms (basis vectors) are replaced by continuous, fully differentiable functions parameterized by neural networks.

these basis functions, as follows:

$$u^{(i)}(x) \approx \sum_{l=1}^Q \alpha_l^{(i)} \psi_l(x) = \Psi^T(x) \alpha^{(i)}, \quad (9)$$

where $\alpha_l^{(i)}$ is the coefficient corresponding to the l -th basis function for the i -th signal realization. Naturally, one would be interested in orthogonal basis functions to eliminate redundancy. This property also enables faster computation at inference since the projection onto orthogonal basis functions can be formulated as a convex optimization problem. Additionally, certain statistical analyses become more straightforward; for instance, the total variance of the random field can be decomposed into the sum of the variances of the individual coefficients. Similarly, this reduction can be applied to statistical moments of higher orders.

Definition 2.3 (Orthogonal Functions). *Two functions $\psi_i(x)$ and $\psi_j(x)$ are orthogonal over the domain x if their inner product $\langle \psi_i, \psi_j \rangle$ is zero for $i \neq j$, i.e.,*

$$\langle \psi_i, \psi_j \rangle \triangleq \int_x \psi_i(x) \psi_j(x) dx = 0, \quad \text{if } i \neq j. \quad (10)$$

These basis functions can be predefined using well-known orthogonal bases, such as Fourier bases or those used in polynomial chaos expansion (PCE) [28, 4, 15, 48, 45]. However, similar to PCA **basis vectors**, it would be more flexible and potentially more efficient if the **basis functions** could be data-dependent. To this end, we parameterize these functions as neural networks $\psi_l(x; \theta_l)$ where θ_l concatenates all parameters associated with the l -th neural network basis function, as follows:

$$u^{(i)}(x) \approx \Psi^T(x; \theta) \alpha^{(i)}, \quad (11)$$

where θ concatenates the parameters of all neural network basis functions. Now, the challenge is to learn the parameterized dictionary $\Psi(x; \theta)$ such that its atoms are orthogonal to each other.

Remark 2.4. In this section, the symbol θ is reused to denote the parameters of the neural networks ψ_l . It is important to note that these parameters are distinct from those used for \mathcal{F}_θ in Section 2.1, despite the notation being the same.

The projection operator $\text{Proj}_\Psi(\cdot) : \mathcal{U} \mapsto \mathbb{R}^{|\Psi|}$ is defined with respect to the dictionary Ψ with $|\Psi|$ number of atoms, which returns the coordinates of the projection of the input function $u(x)$ onto the subspace spanned by the dictionary's basis functions, such that an error measure (in the empirical risk minimization sense) between the original signal and its projection is minimized, as follows,

$$\alpha = \text{Proj}_\Psi[u(x)] \triangleq \underset{\alpha}{\text{argmin}} \|u(x) - \Psi^T(x; \theta) \alpha\|_2^2 + \mathcal{R}(\alpha). \quad (12)$$

Here, the L_2 -norm is chosen as the error measure with respect to a well-defined inner product $\|r(x)\|_2^2 = \langle r(x), r(x) \rangle$, and $\mathcal{R}(\alpha)$ is a regularization term, which can promote sparsity in the solution and/or improve the condition number of the Hessian matrix for optimization, depending on its form. We apply L_2 regularization $\mathcal{R}(\alpha) = \lambda \|\alpha\|_2^2$, where $\lambda \in \mathbb{R}^+$ is a penalty parameter that controls the influence of the regularizer. Hence, one can easily show that the coordinates can be found via,

$$\alpha_l = \text{Proj}_{\psi_l}[u(x)] = \frac{\langle u(x), \psi_l(x) \rangle}{\langle \psi_l(x), \psi_l(x) \rangle + \lambda}; \quad 1 \leq l \leq |\Psi|. \quad (13)$$

For the optimal values, and when $\lambda = 0$, one can easily show that the residual, $r(x) = u(x) - \Psi^T(x; \theta) \alpha$, is orthogonal to the basis functions, hence to the subspace spanned by the dictionary. Therefore, for small values of λ (i.e., $\lambda \rightarrow 0^+$), one can expect the residual to be ‘‘approximately’’ orthogonal to this subspace. In other words, the residual cannot be expressed linearly by the other basis functions. Therefore, the residual can serve as an effective choice for a new basis function to enhance the representation of the data, while maintaining (approximate) orthogonality. This is similar to the vector space viewpoint, where the residual vector is used as a new direction for data representation. This simple yet powerful concept has also been employed in diffusion maps (an unsupervised ML method [27, 10]) to identify unique eigendirections through local linear regression [12]. We utilize this intuitive fact to derive an algorithm that aims to iteratively construct an approximately orthogonal dictionary of atoms as described in Algorithm 1.

Algorithm 1 Dictionary Learning (Batch-wise)

```

1: Input:
2:  $\mathcal{D}_u = \left\{ \mathcal{D}_u^{(i)} \right\}_{i=1}^N$ ,  $\mathcal{D}_u^{(i)} = \left\{ (x^{(i,j)}, \bar{u}^{(i,j)}) \right\}_{j=1}^{M^{(i)}}$  ▷  $N$  realizations of the input function  $\bar{u}(x)$ 
3:  $\Psi = \{1\}$  ▷ A trivial dictionary
4:  $\eta \in \mathbb{R}^+$  ▷ Optimizer learning rate
5:  $0 < \text{Tol.} \ll 1$  ▷ A small target tolerance to be achieved for the reconstruction
6: Output:  $\Psi = \{\psi_l(\cdot; \theta_l)\}_{l=1}^{|\Psi|}$  ▷ A parameterized dictionary by  $|\Psi|$  neural networks
7: while Recon. Err.  $\geq$  Tol. do
8:   Add a randomly initialized neural network basis  $\psi^{\text{new}}(x; \theta^{\text{new}})$  to the dictionary  $\Psi(x; \theta, \theta^{\text{new}})$ 
9:   for  $e \leftarrow 1$  to  $N_{\text{epoch}}$  do
10:    for  $i \leftarrow 1$  to  $N$  do ▷ Loop over realizations
11:       $\alpha^{(i)} = \text{Proj}_{\Psi}[u^{(i)}(x)] \approx \underset{\alpha}{\text{argmin}} \mathbb{E}_{(x, \bar{u}) \sim \mathcal{D}_u^{(i)}} \left\| \bar{u} - \Psi^T(x; \theta, \theta^{\text{new}}) \alpha \right\|_2^2 + \mathcal{R}(\alpha)$ 
12:    end for
13:     $\theta^{\text{new}} \leftarrow \theta^{\text{new}} - \eta \nabla_{\theta^{\text{new}}} \mathbb{E}_i \left[ \mathbb{E}_{(x, \bar{u}) \sim \mathcal{D}_u^{(i)}} \left\| \bar{u}(x) - \Psi^T(x; \theta, \theta^{\text{new}}) \alpha^{(i)} \right\|_2^2 \right]$  ▷ Batch-wise gradient descent
14:    end for
15:    Calculate reconstruction error.
16: end while

```

To promote orthogonality, each time we add a new basis function ψ_{new} , this function is used to capture the expected value of the residual function over the entire dataset. This can be observed in line 13 of the algorithm, as follows:

$$\mathcal{L}(\theta_{\text{new}}) : \bar{u} - \Psi^T(x; \theta, \theta_{\text{new}}) \alpha = \bar{u} - \underbrace{\sum_{l=1}^{|\Psi|-1} \psi_l(x; \theta_l) \alpha_l}_{\text{current residual}} - \psi_{\text{new}}(x; \theta_{\text{new}}) \alpha_{\text{new}}. \quad (14)$$

Note that here the basis functions and their sparse coefficients are unknown, making the optimization challenging. We adopt ideas from the Alternating Direction Method of Multipliers (ADMM) [6] by separating these two unknowns. In the first step (line 11 in Algorithm 1), we assume the basis functions are fixed and find the corresponding coefficients. Then, in the second step (line 13 in Algorithm 1), we assume the coefficients are fixed and optimize the basis functions. This approach bypasses the need for backpropagation through an optimization step in the first stage, which, while possible, can be computationally expensive. Additionally, performing backpropagation through a linear solver with a poorly conditioned kernel (due to inaccurate basis functions) can lead to unstable optimization.

As previously mentioned, the first ADMM step (line 13 in Algorithm 1) can be executed efficiently by appropriately choosing the regularizer and ensuring the orthogonality of the dictionary. Although the L_1 -norm regularizer may be more effective in promoting sparsity, the L_2 -norm regularizer facilitates faster computation and implementation

because the optimization can be formulated as a linear system. Consequently, the dictionary coefficient $\alpha^i \in \mathbb{R}^{|\Psi|}$ for the i -th realization can be found via:

$$\alpha^{(i)} = \left(\Psi^{(i)} \Psi^{(i)T} + \lambda \mathbf{I} \right)^{-1} \Psi^{(i)} \mathbf{U}^{(i)}; \quad \Psi^{(i)} \in \mathbb{R}^{|\Psi| \times M^{(i)}} \quad \mathbf{U}^{(i)} \in \mathbb{R}^{M^{(i)}}, \quad (15)$$

where $\Psi^{(i)}(\mathbf{x}; \theta)$ represents the basis function values at the discretization points of the i -th realization $\{\mathbf{x}^{(i,j)}\}_{j=1}^{M^{(i)}}$, and $\mathbf{U}^{(i)}$ are the i -th realization values at those corresponding points $\{\mathbf{u}^{(i,j)}\}_{j=1}^{M^{(i)}}$. Notice that the kernel of the linear system scales with the dictionary size and not the discretization resolution. Therefore, this implementation is usually more computationally favorable than Eq. (13) which requires numerical integration and scales with the resolution size, particularly in cases where the number of basis functions is much less than the discretization resolution, which is the case in our numerical examples.

We have studied the ability of the proposed algorithm to find appropriate orthogonal basis functions in Appendix F, where we compare our algorithm with classical Gappy PCA or GPOD [13] in identifying basis functions from masked, incomplete data. Moreover, the possibility of using random basis functions is also explored and discussed.

2.2.2 Sample-wise Learning

By assuming the existence of a set of orthogonal basis functions ψ_i whose linear combinations can represent the signals, and since the signals themselves belong to the subspace spanned by these basis functions, it follows that each basis function can be represented as a linear combination of the signals. This is essentially a generalization of the Gram-Schmidt orthogonalization to function spaces, where a new basis function $\psi_{\text{new}}^{\text{gs}}(x)$ is constructed according to a new signal $u_{\text{new}}(x)$ as follows:

$$\psi_{\text{new}}^{\text{gs}}(x) = u_{\text{new}}(x) - \sum_{j=1}^{|\Psi^{\text{gs}}|} \alpha_j^{\text{new}} \psi_j^{\text{gs}}(x), \quad (16)$$

where the right-hand side is the residual between the new signal and its best reconstruction with the current basis functions available in the dictionary. Hence, the coefficients α_j^{new} are the projections of the new signal onto the previously found basis functions $\psi_j^{\text{gs}}(x)$, see Eq. (13). It is straightforward to show that if $u_{\text{new}}(x)$ does not belong to the dictionary subspace, the residual signal $\psi_{\text{new}}^{\text{gs}}(x)$ is orthogonal to the subspace. The complete procedure of constructing an appropriate dictionary with (weakly) orthogonal basis functions parameterized by neural networks is presented in Algorithm 2.

Algorithm 2 Dictionary Learning (Sample-wise)

- 1: **Input:**
 - 2: $\mathcal{D}_u = \left\{ \mathcal{D}_u^{(i)} \right\}_{i=1}^N$, $\mathcal{D}_u^{(i)} = \left\{ (\mathbf{x}^{(i,j)}, \bar{u}^{(i,j)}) \right\}_{j=1}^{M^{(i)}}$ ▷ N realization of the input function $\bar{u}(x)$
 - 3: $\Psi^{\text{gs}} = \emptyset$ ▷ A trivial dictionary
 - 4: $\eta \in \mathbb{R}^+$ ▷ Optimizer learning rate
 - 5: $0 < \text{Tol.} \ll 1$ ▷ A small target tolerance to be achieved for the reconstruction
 - 6: **Output:** $\Psi^{\text{gs}} = \left\{ \psi_l^{\text{gs}}(\cdot; \theta_l) \right\}_{l=1}^{|\Psi^{\text{gs}}|}$ ▷ A parameterized dictionary by $|\Psi^{\text{gs}}|$ neural networks
 - 7: **for** $i \leftarrow 1$ to N **do**
 - 8: $r^{(i)}(\mathbf{x}; \alpha, \theta) = u^{(i)}(\mathbf{x}) - \Psi^{\text{gs}T}(\mathbf{x}; \theta) \alpha$ ▷ The residual function associated with the i -th signal
 - 9: $\alpha^{(i)} = \underset{\alpha}{\operatorname{argmin}} \mathbb{E}_{\mathbf{x} \sim \mathcal{D}_u^{(i)}} \left\| r^{(i)}(\mathbf{x}; \alpha, \theta) \right\|_2^2 + \mathcal{R}(\alpha)$ ▷ The best estimator of basis coefficients
 - 10: $\text{Err} = \mathbb{E}_{\mathbf{x} \sim \mathcal{D}_u^{(i)}} \left\| r^{(i)}(\mathbf{x}; \alpha^{(i)}, \theta) \right\|_2^2$ ▷ The estimated residual norm of the best estimator
 - 11: **if** $\text{Err.} \leq \text{Tol.}$ **then** ▷ Check if the reconstruction error is satisfactory
 - 12: **continue**
 - 13: **end if**
 - 14: $\theta_{\text{new}} = \underset{\theta}{\operatorname{argmin}} \mathbb{E}_{(\mathbf{x}, \bar{u}) \sim \mathcal{D}_u^{(i)}} \left\| \psi_{\text{new}}^{\text{gs}}(\mathbf{x}; \theta) - r^{(i)}(\mathbf{x}; \alpha^{(i)}, \theta) \right\|_2^2$ ▷ Train a new basis to capture the residual signal
 - 15: $\Psi^{\text{gs}} \leftarrow \Psi^{\text{gs}} \cup \left\{ \psi_{\text{new}}^{\text{gs}}(\mathbf{x}; \theta_{\text{new}}) \right\}$ ▷ Update the dictionary
 - 16: **end for**
-

Discussion: Computational Complexity and Efficiency – Although these two algorithms share similarities, they may have different computational costs and training stability. For example, time complexity of Algorithm 2 scales

linearly with the number of realizations, which can be mitigated by the batch-wise training feature of Algorithm 1. Additionally, the basis functions identified by Algorithm 2 may be more sensitive to the order of the data stream since the first basis is derived from the first data it encounters. Moreover, when the data per realization is severely sparse, this algorithm may produce initial basis functions that are overfitted and not representative of the entire set of realizations. Consequently, under such scenarios, the initial basis functions may introduce highly oscillatory components, leading to noisy information during the basis identification for other realizations, which do not reflect the statistical properties of the entire dataset. The answer to all these questions requires a separate study and comparison between these two algorithms under various scenarios, which is beyond the main focus of this research. Hence, in this work, we primarily focus on the application of Algorithm 1 and only showcase the application of Algorithm 2 in the final numerical example.

Discussion: Normalization – From a theoretical perspective, the introduced algorithms aim to (weakly) enforce orthogonality of the identified basis functions. However, for several reasons, one might be interested in basis functions that are normalized as well, i.e., orthonormal basis functions. One reason could be attributed to potential identifiability issues associated with Eq. (11), where both the basis functions and coefficients are unknown. If one scales up the coefficients by a factor and simultaneously scales down the basis functions by the same factor, the same representation can be achieved, although the unknowns themselves have changed. The ADMM method mitigates this issue by solving for each unknown separately while fixing the others, thereby preventing simultaneous changes. However, controlling the scale or norm of either set of unknowns may further suppress such potential issues. Also, the relative scale of each basis function compared to others may impact the scale of its corresponding optimal coefficient relative to the coefficients of other basis functions. Since we may later use the basis coefficients in other downstream tasks (here, operator learning), it may be helpful to have learned bases with relatively the same scaling or norm. This way, the scale of their corresponding coefficients will have a particular meaning in terms of their relative importance in the prediction (coefficients with higher values indicate that their corresponding bases have more impact in the prediction). Several strategies are possible for the normalization of the learned basis functions: (1) one may use a normalization layer in the output layer of the neural network *during* the training to adjust the basis functions according to the batch statistics. In this study, we used an L_2 -norm normalization layer of this type, where the normalized basis is $\psi_{\text{norm}}(\mathbf{x}; \boldsymbol{\theta}) = \psi(\mathbf{x}; \boldsymbol{\theta}) / \sqrt{\mathbb{E}_x[\psi^2(\mathbf{x}; \boldsymbol{\theta})]}$. This type of normalization shares similarities with other batch-wise normalization layers commonly used in ML [1, 49]. (2) If the batch statistics of the given data do not accurately represent the actual statistics, one may normalize the learned basis *after* its training. To do this, a sufficiently large number of points can be artificially generated to empirically estimate the norm of the current un-normalized basis function, using a Markov Chain Monte Carlo (MCMC) estimate. This scaling factor can then be saved for later use before proceeding to learn the next basis function. In this work, we used the first approach in our numerical examples unless otherwise specified.

2.3 Parameterization via Implicit Neural Representation

In this section, we provide details on how we chose the neural network parameterization for the unknown basis functions introduced in the previous section.

Use cases of INRs in the literature mostly deal with modeling the signal itself directly. However, in this work, instead of applying the INRs directly to the signal $u(\mathbf{x})$, we apply them to the basis functions $\psi_l(\mathbf{x})$, which serve as templates for modeling $u(\mathbf{x})$. One challenge in utilizing INRs is that conventional MLPs, despite their universal approximation property [18], struggle to learn fine details or high-frequency content due to a phenomenon known as spectral bias [30]. Several recent works aim to address this issue by modifying the conventional MLP architecture. Two prominent approaches include using sinusoidal activation functions, known as the SIREN approach [36], and incorporating random Fourier features in the first layer of the MLP, known as positional encoding [26, 41, 31]. Here, we use the SIREN approach to parameterize each newly added basis function $\psi_l(\mathbf{x}; \boldsymbol{\theta}_l)$ in Algorithm 1 due to its simplicity and the extensive success reported in various computer vision tasks [36, 8, 47].

We parameterize each basis function $\psi_l(\mathbf{x})$ using a SIREN MLP with n hidden layers as follows:

$$\psi_l(\mathbf{x}; \boldsymbol{\theta}_l) = \mathbf{W}_{n+1}^{(l)} (\phi_n \circ \phi_{n-1} \cdots \phi_1)(\mathbf{x}) + \boldsymbol{\beta}_{n+1}^{(l)}; \quad \phi_m(\mathbf{h}_{m-1}^{(l)}) \triangleq \sin\left(\mathbf{W}_m^{(l)} \mathbf{h}_{m-1}^{(l)} + \boldsymbol{\beta}_m^{(l)}\right), \quad (17)$$

where $\mathbf{h}_m^{(l)}$ denotes the m -th hidden state, with $h_0 \triangleq \mathbf{x}$ and $0 \leq m \leq n$. $\mathbf{W}_m^{(l)}$ and $\boldsymbol{\beta}_m^{(l)}$ represent the typical weights and biases of the MLP, respectively. The vector $\boldsymbol{\theta}_l$ concatenates all the trainable parameters of the SIREN, i.e., $\boldsymbol{\theta}_l \equiv \left\{ \mathbf{W}_m^{(l)}, \boldsymbol{\beta}_m^{(l)} \right\}_{m=1}^{n+1}$. The convergence and accuracy of the SIREN depend on the appropriate initialization of the trainable parameters. Following the method proposed by [36], we initialize the weights drawn from a uniform distribution $\mathbf{W}_m \sim \text{Uniform}[-\omega_0 \sqrt{6/\dim(\mathbf{h}_{m-1})}, \omega_0 \sqrt{6/\dim(\mathbf{h}_{m-1})}]$ where $\omega_0 = 1$ for all layers except the first layer, in which it is a hyperparameter that depends on the problem at hand. This ensures that the pre-activations are

normally distributed with unit variance, leading to more stable training by preventing vanishing or exploding gradients. The biases are set to zero during the initialization stage.

Remark 2.5. Although INRs could be more memory efficient per instance (e.g., an image) signal compression, their vanilla use case may not seem ideal when dealing with many instances. This is because each instance requires a separate INR with different parameters to be trained from scratch, without leveraging any information obtained from other instances or any potential common structures across instances. Notice that each training of an INR involves solving a **non-convex** optimization problem, which is typical for deep neural network training. One approach currently under exploration is to use meta-learning for better initialization of each INR, leading to fewer iterations, or some form of parameter sharing across instances [35, 40]. However, as explained, in our approach we do not directly model signals with INRs. Instead, we learn a dictionary of basis functions as INRs in an *offline* manner, which indirectly captures the common structure across instances. Then, at inference or for an unseen signal, we only solve a **convex** optimization problem to find the coefficients of the INR basis. This eliminates the need to introduce or train a new INR from scratch. In that regard, using INRs as basis functions may offer new ways to reduce the computational burden during inference when dealing with implicit representations of signals; however, this is not the focus of the current work.

3 Numerical Examples

In this section, we showcase the resolution independence of RINO by solving four numerical examples, where the data is synthesized from PDE solutions under different setups, ranging from 1D operators to operators with different supports in their input and output functions. The setup for the data generation and operator learning task is specified for each problem separately in their respective sections. Examples in Sections 3.1.1 to 3.1.4 are chosen from the literature or designed to verify the resolution independence of RINO with respect to the input function data, which is the main focus of this study. Example in Section 3.2 is designed to demonstrate the application of RINO in a more challenging scenario where the data realizations are obtained from finite element simulations of varying resolutions. The compactness and consistency of the vectorial representation achieved through our dictionary learning algorithm are discussed and studied in comparison with random projections in Appendix F.

In cases where the PDE solver for data generation works on a fixed discretization, we randomly select only a subset of input function sensors for training to showcase RINO’s ability to handle irregular data. The locations and numbers of these sensors vary from sample to sample. Assuming an input function realization is discretized at M points, a corresponding “random” realization with random discretization is identified by randomly selecting M_{rand} points without replacement, where M_{rand} is independently drawn for each realization from the uniform distribution $M_{\text{rand}} \sim \text{Uniform}[M_{\text{min}}, M_{\text{max}}]$, and $0 < M_{\text{min}} < M_{\text{max}} \leq M$.

Since the input and output functions may have different scales across realizations, we use the relative mean square error (RMSE) as the training loss function. This approach is suggested to facilitate training and improve accuracy in operator learning problems [42, 22]. Consequently, all reported errors are based on the relative MSE measure, as follows:

$$\text{Err}(v, v^{\text{pred}}) = \mathbb{E}_{v \sim \mu_v} \frac{\|v - v^{\text{pred}}\|_2^2}{\|v\|_\infty^2}. \quad (18)$$

3.1 Verification Examples

3.1.1 Example 1: Antiderivative

The first verification example is taken from [22]. In this example, the data is generated according to the following antiderivative operator:

$$\frac{ds}{dx} = u(x); \quad x \in [0, 1] \quad (19)$$

where $u(x)$ is modeled as a Gaussian random process with zero mean and a covariance function defined by the radial basis function (RBF) with length scale $l = 0.2$, i.e., $u(x) \sim \mathcal{GP}(0, \text{Cov}(x_1, x_2))$; details are provided in Appendix G. We use the open-source dataset from [22], which includes 150 pairs of input-output functions for the training set and 1000 pairs for the test set. In the original dataset, the functions are discretized at 100 equally spaced sensor points. Following the procedure described earlier, we set $M_{\text{min}} = 10$ and $M_{\text{max}} = 60$ to generate random point clouds for the training and testing cases. In other words, each training data function has a randomly subsampled discretization of between 10 and 60 points.

As described in the formulation section, the first step in RINO is to learn a dictionary to represent the input functions. This dictionary will be used to find embedding coordinates for the operator learning task, specifically for use in the

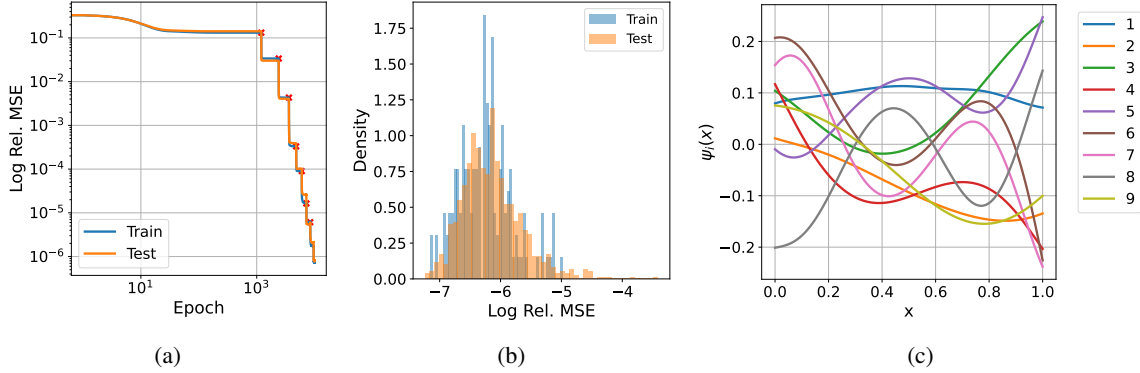


Figure 4: Antiderivate Example: (a) Loss function during optimization iterations for dictionary learning of the input function bases. (b) Distribution of reconstruction errors for the train and test datasets after training. (c) The learned basis functions in the dictionary.

branch network. Figure 4(a) shows the reconstruction errors in Algorithm 1 during the ADAM [19] iterations. Each red cross on the curve indicates the step at which a new basis function is added (line 8 in Algorithm 1). With a total of 9 learned basis functions, the data can be reconstructed with high accuracy, as shown by the distribution of errors in Figure 4(b) for both training and testing datasets. The learned basis functions are plotted in Figure 4(c).

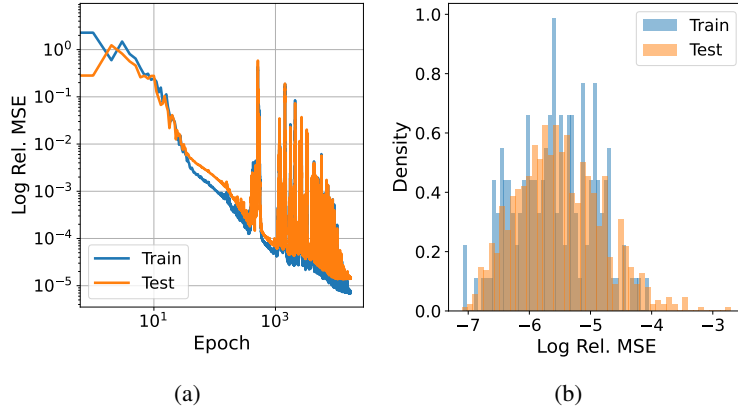


Figure 5: Antiderivate Example: (a) Loss function during optimization iterations for operator learning. (b) Distribution of output function prediction errors for the training and testing datasets after training.

The ADAM iterations for operator learning using the input function embeddings obtained from the learned dictionary are shown in Figure 5(a). The close gap between the training and testing errors during the iterations indicates good generalization behavior, suggesting that the input function representation is informative. In Figure 5(b), the distribution of output function prediction errors after training is shown for both the training and testing sets.

In Figure 6, the prediction of RINO at inference is shown for two queries from the test dataset. Figure 6(a) presents the results for the worst-case output function prediction. The first column shows the queried input function, which includes a point cloud with 35 random data points shown as ‘o’ along with the masked data points shown as ‘x’ that are not provided to the dictionary but are used to assess the accuracy of the reconstruction. The second column shows the projection coefficients of the input function data onto the learned dictionary, which has a total of 9 basis functions. The reconstruction using these coefficients is also plotted in the first figure. The last column shows the prediction of the output function along with the true model solution. Similarly, Figure 6(b) presents the same results for the test sample at the 25th percentile of the error distribution, meaning 75% of test cases have lower error than this sample. As the results show, the RINO method demonstrates good performance in providing predictions at inference for input function data recorded at an arbitrary (but sufficiently rich) number of sensors and locations.

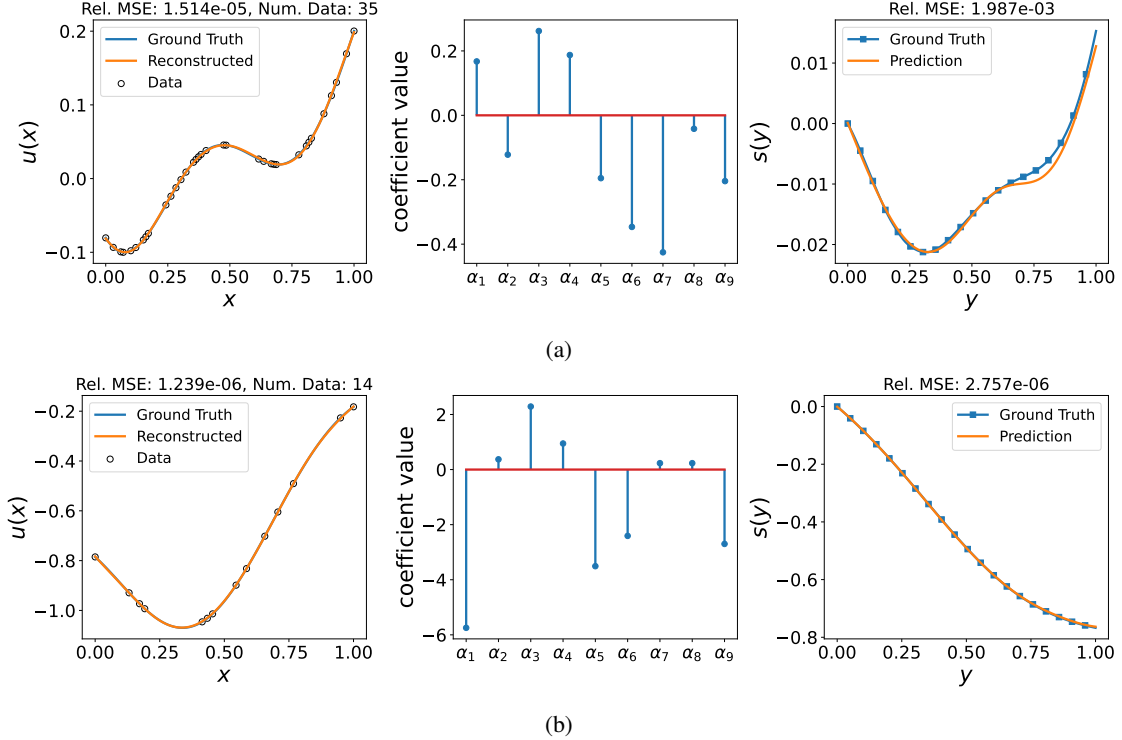


Figure 6: Antiderivative Example: RINO prediction for two queried input functions at inference and for the testing dataset: (a) Worst-case sample with the highest error in output function prediction, (b) Sample at the 25th percentile of the error distribution (i.e., 75% of cases have less error than this value). The first column shows the queried input function data as ‘o’ and the masked points (not provided to the dictionary) as ‘x’, along with the reconstruction from dictionary learning. The second column shows the projection coefficients of the queried input function data onto the learned dictionary of basis function from Figure 4(c). The last column shows the output function prediction along with the true solution.

3.1.2 Example 2: Nonlinear 1D Darcy’s Equation

In this example, we increase the complexity of the previous problem by introducing a nonlinear operator. A variant of the nonlinear 1D Darcy’s equation is given by the following form:

$$\frac{ds}{dx} \left(-\kappa(s(x)) \frac{ds}{dx} \right) = u(x); \quad x \in [0, 1], \quad (20)$$

where the solution-dependent permeability is $\kappa(s(x)) = 0.2 + s^2(x)$ and the source term is a random field $u(x) \sim \mathcal{GP}$ with length scale $l = 0.05$. Homogeneous Dirichlet boundary conditions $s = 0$ are defined at the domain boundaries. The FEniCS finite element solver [2] is used to generate data by discretizing the domain into 50 uniformly spaced nodal points. Following the procedure described earlier, we set $M_{\min} = 20$ and $M_{\max} = 35$ to generate random point clouds for the training and testing cases. The sizes of the training and test datasets are 800 and 200, respectively.

The worst-case RINO predictions are shown in Figure 7(a), demonstrating visually acceptable accuracy for both the output function prediction and the input function reconstruction. Similarly the test sample at the 25th percentile of the error distribution is shown in Figure 7(b).

3.1.3 Example 3: Nonlinear 2D Darcy’s Equation

In this example, we extend the previous problem to a two-dimensional setting. The nonlinear Darcy’s equation in two dimensions is given by:

$$\nabla \cdot (-\kappa(s(\mathbf{x})) \nabla s) = u(\mathbf{x}); \quad \mathbf{x} \in [0, 1]^2, \quad (21)$$

where the solution-dependent permeability is $\kappa(s(\mathbf{x})) = 0.2 + s^2(\mathbf{x})$ and the source term is a random field $u(\mathbf{x}) \sim \mathcal{GP}$ with length scale $l = 0.25$. Homogeneous Dirichlet boundary conditions $s = 0$ are defined at the domain boundaries.

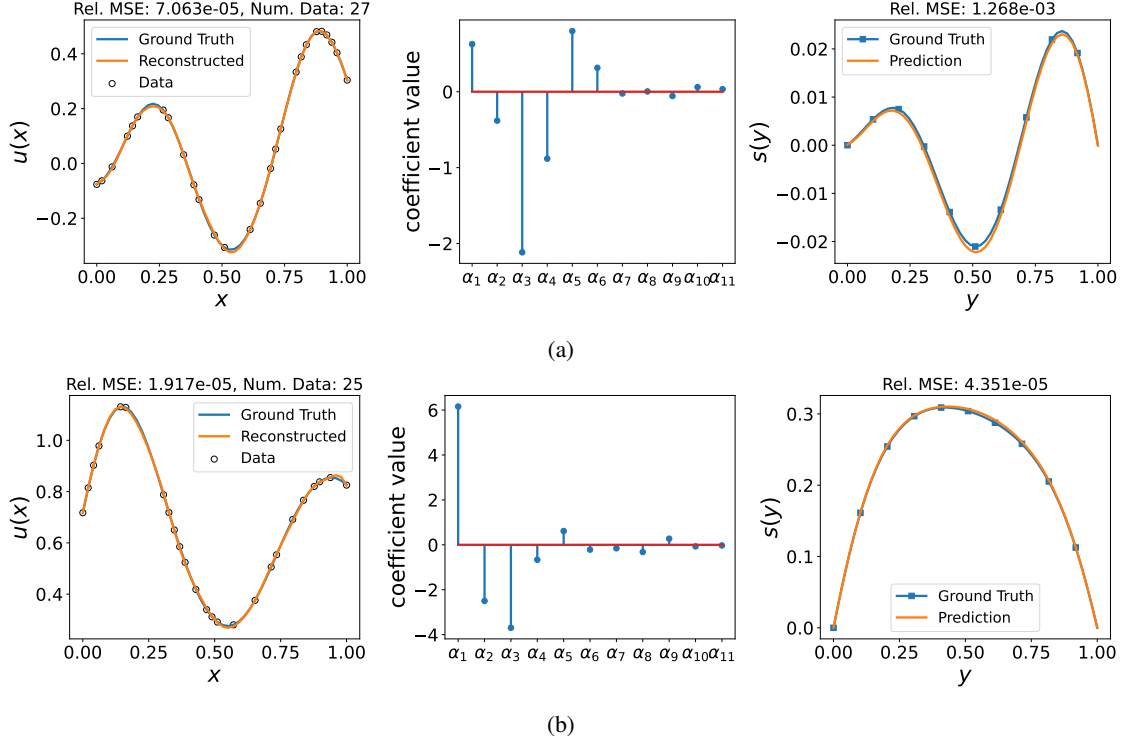


Figure 7: 1D Nonlinear Darcy’s Equation: RINO Prediction for two queried input functions at inference and for the testing dataset: (a) Worst-case sample with the highest error in output function prediction, (b) Sample at the 25th percentile of the error distribution (i.e., 75% of cases have less error than this value). The first column shows the queried input function data as ‘o’ and the masked points (not provided to the dictionary) as ‘x’, along with the reconstruction from dictionary learning. The second column shows the projection coefficients of the queried input function data onto the learned dictionary of basis function from Figure 4(c). The last column shows the output function prediction along with the true solution.

The solution field is obtained via the finite element method. Input function random fields are discretized on a 20×20 uniform grid, while the triangulation of the finite element domain does not necessarily coincide with these input sensor point locations. Following the procedure described earlier, we set $M_{\min} = 100$ and $M_{\max} = 280$ to generate random point clouds over a subset of the 400 grid points for the training and testing cases. The sizes of the training and test datasets are 800 and 200, respectively.

The RINO predictions corresponding to the worst-case test error for the output field is shown in Figure 8, demonstrating satisfactory error.

3.1.4 Example 4: Burgers’ Equation

In this numerical example, we examined an initial boundary value problem in which the input and output functions of the operator have different domains and dimensions. Specifically, we looked at the parametric Burgers’ equation, as introduced in [42], with the random field initial condition $s(x)|_{t=0}$ as the input function and the space-time solution $s(x, t)$ as the output function:

$$\frac{\partial s}{\partial t} + \frac{\partial s}{\partial x} = \nu \frac{\partial^2 s}{\partial x^2}; \quad (x, t) \in [0, 1]^2, \quad (22)$$

$$s|_{t=0} = u(x), \quad (23)$$

where periodic boundary conditions are assumed, and the periodic initial condition is a Gaussian random process with parameters similar to [42], and $\nu = 0.01$. A spectral solver is used to obtain the solution field on a 101×100 grid in the space-time domain for each input function, which is discretized on 101 uniformly spaced points. Following the procedure described earlier, we set $M_{\min} = 40$ and $M_{\max} = 70$ to generate random point clouds for the training and testing cases. The sizes of the training and test datasets are 1500 and 500, respectively. Notice that the input function

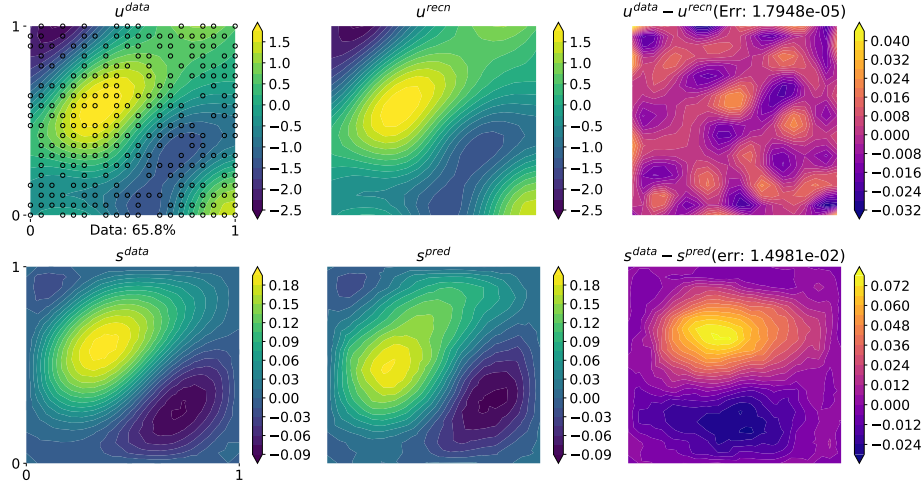


Figure 8: 2D Nonlinear Darcy’s Equation: RINO prediction for the worst-case output function $s(\mathbf{y})$ in the test dataset. The top left figure shows the queried input function data $u(\mathbf{x})$, with black circle symbols indicating the queried data. The middle top figure shows the input field reconstruction via the learned dictionary. The top right figure shows the error between the reconstructed input field and the ground truth. The bottom figures show the output field $s(\mathbf{y})$, the RINO prediction, and its corresponding errors.

samples are randomly discretized; however, the predictions are on the full solution grid for the results in this section, similar to other examples.

To showcase the flexibility of the RINO framework, we use predefined trunk basis vectors as the first 70 POD bases obtained from the solution output snapshots of the training dataset. It has been shown previously that using predefined optimal bases can facilitate the training of DeepONet and achieve faster convergence [23]. Two samples from the testing set are shown in Figure 9.

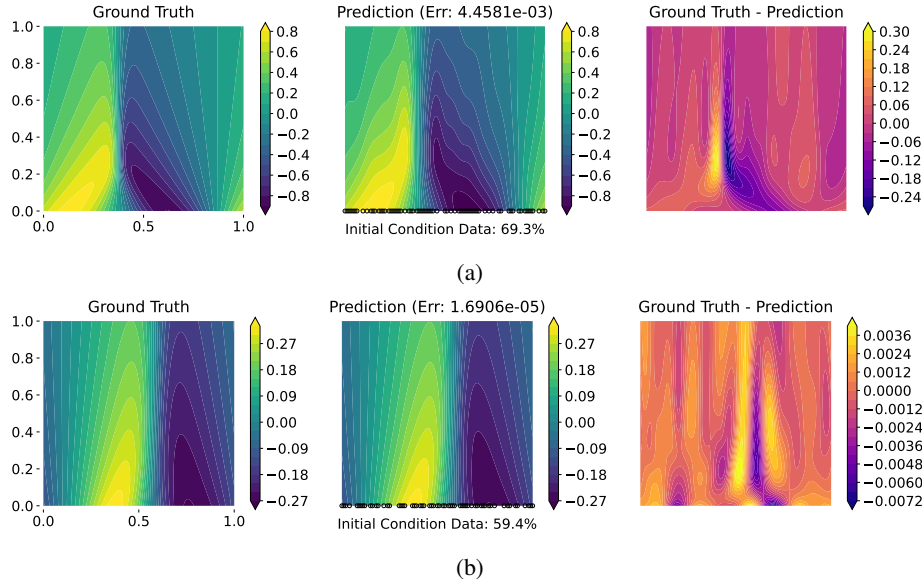


Figure 9: 2D Burger’s Equation: RINO prediction for two queried initial condition fields at inference and for the testing dataset: (a) Sample with the highest error in output function prediction $s(\mathbf{y})$, and (b) Sample at the 25th percentile of the error distribution (i.e., 75% of cases have less error than this value). The first column shows the ground truth solution. The second column shows the RINO prediction with the queried input initial condition points shown along the x -axis. The last column shows the point-wise error. The output domain $\mathbf{y} = (x, t)$ has spatio-temporal coordinates, where the horizontal axis represents space and the vertical axis represents time.

3.1.5 Discussion

After training each of the models listed above on the defined randomly sub-sampled data, we can perform inference during testing using any combination of input function sensors and at any desired points, thanks to the fully continuous nature of the RINO for processing both input and output functions. To examine the influence of discretization, we perform additional tests on regularly subsampled sensors for the input function at inference. A summary of our results is provided in Table 1. Rows in this table with a numeric value for the number of sensors (e.g., $M = 100$) indicate performance during inference for input functions queried at structured and uniformly spaced sensor locations. Rows in the table denoted ‘random,’ correspond to test sets on the randomly sub-sampled discretizations described in Sections 3.1.1 – 3.1.4. The RINO used for predictions is trained using a data set of randomly sub-sampled points as described for each problem in Sections 3.1.1 – 3.1.4. Therefore, training error is reported only for the ‘random’ case.

The error statistics shown in Table 1 are computed for the trained models described above. Each neural network model is randomly initialized before training, and the sensor locations for the input functions are also randomly generated for each training run.

As the results suggest, the output function prediction is nearly insensitive to the discretization resolution of the queried input function for all PDE cases. However, in the 1D Nonlinear Darcy’s and Burgers’ equations, we observe a degradation in accuracy after some level of resolution coarsening (see the last row for each case). This occurs because, as anticipated, when the resolution falls below a certain threshold—particularly when it is significantly less than the problem’s characteristic length scale—the predictions become erroneous and thus resolution-dependent. In other words, these correspond to cases where a ReNO cannot be accurately identified due to under-sampling.

	Number of Sensors (M)	Test Error (mean \pm std)	Train Error
Antiderivative			
	random	1.751e-05 \pm 3.398e-06	7.044e-06 \pm 4.122e-07
	100	1.456e-05 \pm 3.126e-06	-
	51	1.198e-05 \pm 1.439e-06	-
	26	1.107e-05 \pm 4.244e-07	-
	21	1.104e-05 \pm 3.037e-07	-
	11	1.238e-05 \pm 6.151e-07	-
Nonlinear Darcy (1D)			
	random	3.630e-05 \pm 7.164e-06	1.390e-05 \pm 1.628e-06
	50	2.989e-05 \pm 5.290e-06	-
	26	3.018e-05 \pm 5.431e-06	-
	11	4.721e-05 \pm 7.422e-06	-
	6	8.347e-03 \pm 5.425e-03	-
Nonlinear Darcy (2D)			
	random	1.121e-03 \pm 1.456e-04	9.261e-04 \pm 2.344e-04
	20 \times 20	1.135e-03 \pm 1.423e-04	-
	10 \times 10	1.135e-03 \pm 1.394e-04	-
	4 \times 4	1.368e-03 \pm 2.039e-04	-
Burgers			
	random	3.795e-05 \pm 1.986e-06	1.361e-05 \pm 9.999e-07
	101	3.789e-05 \pm 1.989e-06	-
	51	3.788e-05 \pm 1.991e-06	-
	21	3.790e-05 \pm 1.986e-06	-
	11	7.011e-04 \pm 3.537e-04	-

Table 1: Resolution dependence study for each verification problem. RINO output function prediction errors are reported for queried input functions at various resolutions denoted by the Number of Sensors (M). Cases where a numerical value is prescribed correspond to fixed regular discretizations of the input. Cases denoted ‘random’ indicate a random subsampling of the input discretization as defined in Sections 3.1.1 – 3.1.4. Mean training/test errors and standard deviations are computed from five independent trials.

3.2 Demonstration Example: Nonlinear 2D Darcy’s Equation on Unstructured Meshes

In this problem, we revisit the 2D Darcy flow problem previously introduced in Section 3.1.3. The main difference is that, in this example, the data belongs to unstructured finite element meshes that differ from realization to realization. The goal here is not to showcase the method’s consistency across varying resolutions (from low to high or vice versa), which was studied in previous problems. Instead, we aim to demonstrate that the RINO can perform operator learning for problems of practical interest involving arbitrary finite element meshes.

To generate training data, we purposely generate unstructured triangular meshes with varying density per realization. The areas with higher mesh density are arbitrary and do not correspond, for example, to areas where the mesh might be refined based on an error estimator. We then interpolate the previously generated random input fields (see Section 3.1.3) onto the new unstructured meshes and obtain the solution field for each realization using a nonlinear finite element solver written in FEniCS [2].

Operator Learning with unknown trunk Similar to the previous examples, using Algorithm 1, we learn 40 INR basis functions to effectively project an arbitrary input function point cloud onto the dictionary subspace with a satisfactory reconstruction error (see Appendix D). We then use this 40-dimensional latent representation for operator learning where the trunk and branch neural networks are unknown and are trained. The worst-case output function prediction and the case corresponding to the 25th percentile of the error distribution from the unseen test data are shown in Figures 10 and 11, respectively. The results indicate a satisfactory training process and prediction capability. The full error distributions for the training and test data are provided in Appendix D.

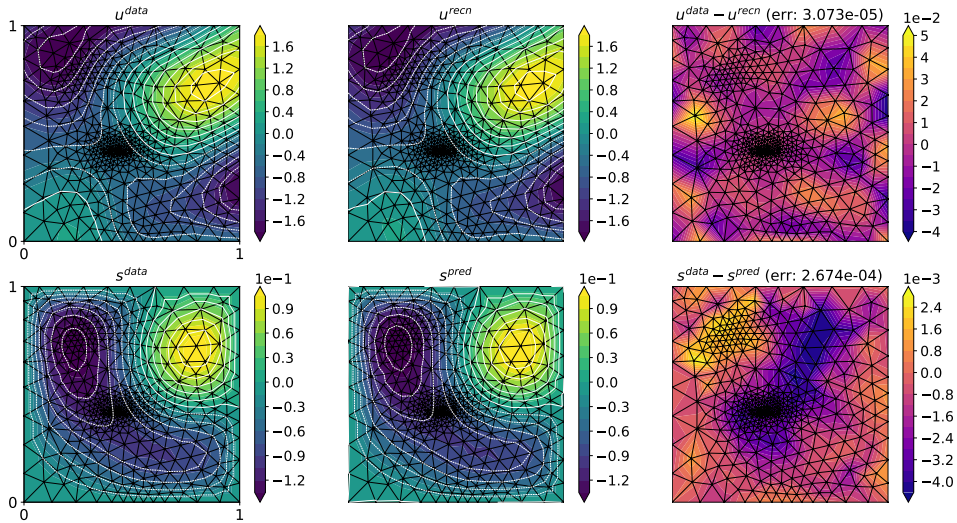


Figure 10: 2D Nonlinear Darcy’s Equation (Unstructured Mesh): RINO prediction with the worst-case output function, $s(\mathbf{y})$, in the test dataset. The top left figure shows the queried input function data $u(\mathbf{x})$. The middle top figure shows the input field reconstruction via learned dictionary. The top right figure shows the error between the reconstructed input field and the ground truth. The bottom figures show the true output field $s(\mathbf{y})$, the RINO prediction, and its corresponding errors.

Operator Learning with predefined INR trunk As discussed in Section 2.1.1, the proposed dictionary learning algorithms can be applied in a similar manner for learning appropriate basis functions for the output function data. Once the dictionary is learned (*offline*), it can be utilized as a predefined trunk. Under such a setup, we only need to train the branch network. In this problem, we utilize Algorithm 2 to learn a dictionary of 54 INR basis functions that can sufficiently approximate the output function data. The worst-case output function prediction and the case corresponding to the 25th percentile of the error distribution from the unseen test data are shown in Figures 12 and 13, respectively. The results indicate a satisfactory training process and prediction capability. The full error distributions for the training and test data are provided in Appendix D.

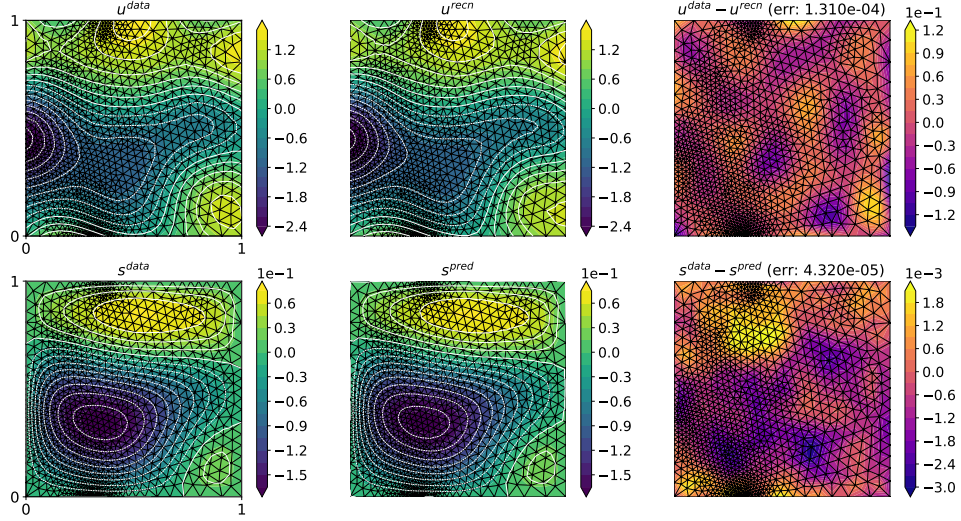


Figure 11: 2D Nonlinear Darcy’s Equation (Unstructured Mesh): RINO results for the test sample with an output function prediction error in the 25th percentile of the error distribution. The top left figure shows the queried input function data $u(\mathbf{x})$. The middle top figure shows the input field reconstruction via learned dictionary. The top right figure shows the error between the reconstructed input field and the ground truth. The bottom figures show the true output field $s(\mathbf{y})$, the RINO prediction, and its corresponding errors.

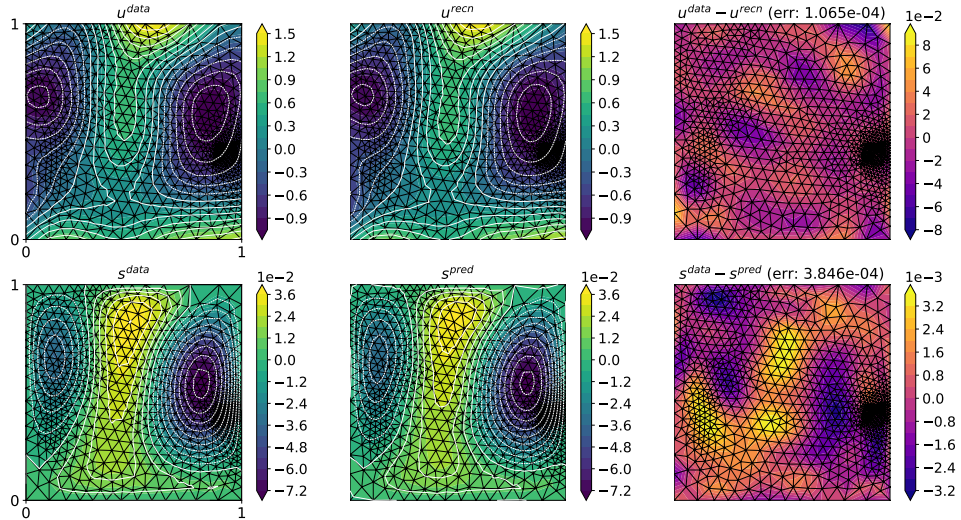


Figure 12: 2D Nonlinear Darcy’s Equation (Unstructured Mesh) with Predefined INR Trunk Net: RINO prediction with the worst-case output function, $s(\mathbf{y})$, in the test dataset. The top left figure shows the queried input function data $u(\mathbf{x})$. The middle top figure shows the input field reconstruction via learned dictionary. The top right figure shows the error between the reconstructed input field and the ground truth. The bottom figures show the true output field $s(\mathbf{y})$, the RINO prediction, and its corresponding errors.

4 Conclusion

In this work, we propose a resolution-independent neural operator (RINO) that modifies the DeepONet formulation with minimal architectural changes to directly work on (sufficiently rich) point clouds sampled from input and output functions without any underlying structural assumptions on the data structure. Specifically, we introduce a dictionary learning algorithm to identify appropriate continuous and fully differentiable basis functions for input function realizations. This allows us to construct an appropriate coordinate system (frame) to project input function point clouds onto, and use the resulting coordinates as the input function representation, which can be subsequently used in the vanilla

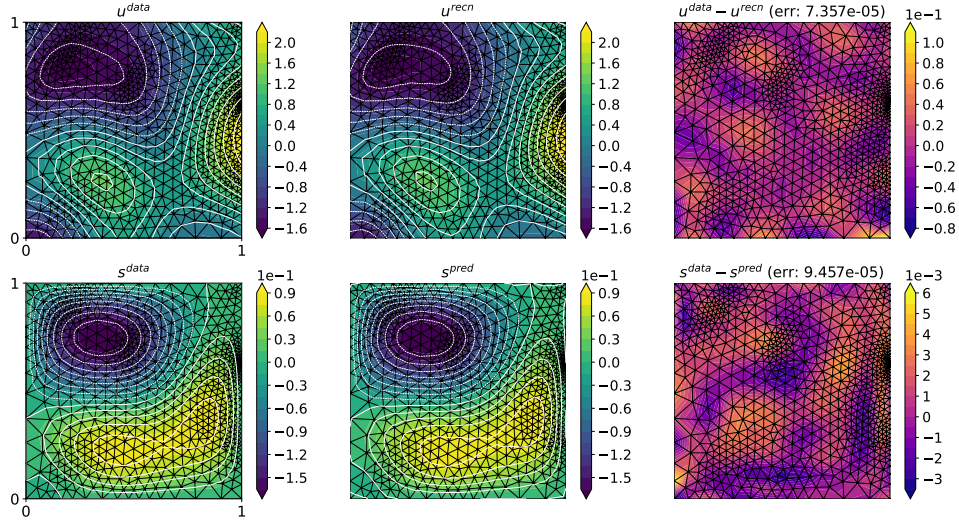


Figure 13: 2D Nonlinear Darcy’s Equation (Unstructured Mesh) with Predefined Trunk Net: RINO results for the test sample with an output function prediction error in the 25th percentile of the error distribution. The top left figure shows the queried input function data $u(\mathbf{x})$. The middle top figure shows the input field reconstruction via learned dictionary. The top right figure shows the error between the reconstructed input field and the ground truth. The bottom figures show the true output field $s(\mathbf{y})$, the RINO prediction, and its corresponding errors.

DeepONet. The application of the introduced algorithm extends beyond the operator learning task and can be used for reconstruction tasks from incomplete or missing information, similar to GPOD. This algorithm can be considered a reconstruction method over function spaces rather than vector spaces, as is the case with GPOD or PCA.

We have empirically studied and demonstrated the resolution independence of the proposed operator learning scheme by solving several numerical experiments from the literature and newly designed ones. Different aspects of the algorithm have been discussed and particularly compared with GPOD.

The introduced algorithm for finding a resolution-independent representation of the input function data has two additional advantages that “come for free”. First, if there is an underlying lower-dimensional structure for the realizations, the algorithm can identify it and reduce the dimensionality of the input function data. This was demonstrated in all our numerical examples. For instance, in one example, the data dimensionality was 100, and we achieved a relatively low reconstruction error using only around 10 basis functions. This compact data representation can directly reduce the size of the branch network. Moreover, such reduced dimensions are more suited for uncertainty quantification and propagation. Second, the reconstruction error can naturally serve as a good estimate of out-of-sample or distribution indicators, which can be leveraged for data acquisition and experiment design.

5 Acknowledgements

We acknowledge the discussion with Professor George E. Karniadakis during the CRUNCH seminar, who brought random projection and ReNO [3] to our attention, which improved our work. This material is based upon work supported by the U.S. Department of Energy, Office of Science, Office of Advanced Scientific Computing Research, under Award Number DE-SC0024162.

References

- [1] Jimmy Lei Ba, Jamie Ryan Kiros, and Geoffrey E Hinton. Layer normalization. *arXiv preprint arXiv:1607.06450*, 2016.
- [2] Igor A. Baratta, Joseph P. Dean, Jørgen S. Dokken, Michal Habera, Jack S. Hale, Chris N. Richardson, Marie E. Rognes, Matthew W. Scroggs, Nathan Sime, and Garth N. Wells. DOLFINx: the next generation FEniCS problem solving environment. preprint, 2023.

- [3] Francesca Bartolucci, Emmanuel de Bézenac, Bogdan Raonic, Roberto Molinaro, Siddhartha Mishra, and Rima Alaifari. Representation equivalent neural operators: a framework for alias-free operator learning. *Advances in Neural Information Processing Systems*, 36, 2024.
- [4] Géraud Blatman and Bruno Sudret. Adaptive sparse polynomial chaos expansion based on least angle regression. *Journal of computational Physics*, 230(6):2345–2367, 2011.
- [5] Nikolas Borrel-Jensen, Somdatta Goswami, Allan P Engsig-Karup, George Em Karniadakis, and Cheol-Ho Jeong. Sound propagation in realistic interactive 3d scenes with parameterized sources using deep neural operators. *Proceedings of the National Academy of Sciences*, 121(2):e2312159120, 2024.
- [6] Stephen Boyd, Neal Parikh, Eric Chu, Borja Peleato, and Jonathan Eckstein. Distributed optimization and statistical learning via the alternating direction method of multipliers. *Foundations and Trends® in Machine Learning*, 3(1):1–122, 2011.
- [7] Qianying Cao, Somdatta Goswami, Tapas Tripura, Souvik Chakraborty, and George Em Karniadakis. Deep neural operators can predict the real-time response of floating offshore structures under irregular waves. *Computers & Structures*, 291:107228, 2024.
- [8] Eric R Chan, Marco Monteiro, Petr Kellnhofer, Jiajun Wu, and Gordon Wetzstein. pi-gan: Periodic implicit generative adversarial networks for 3d-aware image synthesis. In *Proceedings of the IEEE/CVF conference on computer vision and pattern recognition*, pages 5799–5809, 2021.
- [9] Tianping Chen and Hong Chen. Universal approximation to nonlinear operators by neural networks with arbitrary activation functions and its application to dynamical systems. *IEEE Transactions on Neural Networks*, 6(4):911–917, 1995.
- [10] Ronald R Coifman and Stéphane Lafon. Diffusion maps. *Applied and computational harmonic analysis*, 21(1):5–30, 2006.
- [11] P Clark Di Leoni, Lu Lu, Charles Meneveau, George Karniadakis, and Tamer A Zaki. Deepnet prediction of linear instability waves in high-speed boundary layers. *arXiv preprint arXiv:2105.08697*, 2021.
- [12] Carmeline J Dsilva, Ronen Talmon, Ronald R Coifman, and Ioannis G Kevrekidis. Parsimonious representation of nonlinear dynamical systems through manifold learning: A chemotaxis case study. *Applied and Computational Harmonic Analysis*, 44(3):759–773, 2018.
- [13] Richard Everson and Lawrence Sirovich. Karhunen–loève procedure for gappy data. *JOSA A*, 12(8):1657–1664, 1995.
- [14] Bosco García-Archilla, Julia Novo, and Edriss S Titi. Postprocessing the galerkin method: a novel approach to approximate inertial manifolds. *SIAM journal on numerical analysis*, 35(3):941–972, 1998.
- [15] Roger G Ghanem and Pol D Spanos. *Stochastic finite elements: a spectral approach*. Courier Corporation, 2003.
- [16] Alexander N Gorban, Ivan Yu Tyukin, Danil V Prokhorov, and Konstantin I Sofeikov. Approximation with random bases: Pro et contra. *Information Sciences*, 364:129–145, 2016.
- [17] Somdatta Goswami, Minglang Yin, Yue Yu, and George Em Karniadakis. A physics-informed variational deepnet for predicting crack path in quasi-brittle materials. *Computer Methods in Applied Mechanics and Engineering*, 391:114587, 2022.
- [18] Kurt Hornik, Maxwell Stinchcombe, and Halbert White. Multilayer feedforward networks are universal approximators. *Neural networks*, 2(5):359–366, 1989.
- [19] Diederik P Kingma and Jimmy Ba. Adam: A method for stochastic optimization. *arXiv preprint arXiv:1412.6980*, 2014.
- [20] Eleni D Koronaki, Nikolaos Evangelou, Cristina P Martin-Linares, Edriss S Titi, and Ioannis G Kevrekidis. Non-linear dimensionality reduction then and now: Aims for dissipative pdes in the ml era. *Journal of Computational Physics*, 506:112910, 2024.
- [21] Zongyi Li, Nikola Kovachki, Kamyar Aizzadenesheli, Burigede Liu, Kaushik Bhattacharya, Andrew Stuart, and Anima Anandkumar. Fourier neural operator for parametric partial differential equations. *arXiv preprint arXiv:2010.08895*, 2020.
- [22] Lu Lu, Pengzhan Jin, Guofei Pang, Zhongqiang Zhang, and George Em Karniadakis. Learning nonlinear operators via deepnet based on the universal approximation theorem of operators. *Nature machine intelligence*, 3(3):218–229, 2021.
- [23] Lu Lu, Xuhui Meng, Shengze Cai, Zhiping Mao, Somdatta Goswami, Zhongqiang Zhang, and George Em Karniadakis. A comprehensive and fair comparison of two neural operators (with practical extensions) based on fair data. *Computer Methods in Applied Mechanics and Engineering*, 393:114778, 2022.

- [24] Julien Mairal, Michael Elad, and Guillermo Sapiro. Sparse representation for color image restoration. *IEEE Transactions on image processing*, 17(1):53–69, 2007.
- [25] Lars Mescheder, Michael Oechsle, Michael Niemeyer, Sebastian Nowozin, and Andreas Geiger. Occupancy networks: Learning 3d reconstruction in function space. In *Proceedings of the IEEE/CVF conference on computer vision and pattern recognition*, pages 4460–4470, 2019.
- [26] Ben Mildenhall, Pratul P Srinivasan, Matthew Tancik, Jonathan T Barron, Ravi Ramamoorthi, and Ren Ng. Nerf: Representing scenes as neural radiance fields for view synthesis. *Communications of the ACM*, 65(1):99–106, 2021.
- [27] Boaz Nadler, Stéphane Lafon, Ronald R Coifman, and Ioannis G Kevrekidis. Diffusion maps, spectral clustering and reaction coordinates of dynamical systems. *Applied and Computational Harmonic Analysis*, 21(1):113–127, 2006.
- [28] Lukáš Novák, Himanshu Sharma, and Michael D Shields. Physics-informed polynomial chaos expansions. *Journal of Computational Physics*, 506:112926, 2024.
- [29] Bruno A Olshausen and David J Field. Sparse coding with an overcomplete basis set: A strategy employed by v1? *Vision research*, 37(23):3311–3325, 1997.
- [30] Nasim Rahaman, Aristide Baratin, Devansh Arpit, Felix Draxler, Min Lin, Fred Hamprecht, Yoshua Bengio, and Aaron Courville. On the spectral bias of neural networks. In *International conference on machine learning*, pages 5301–5310. PMLR, 2019.
- [31] Ali Rahimi and Benjamin Recht. Random features for large-scale kernel machines. *Advances in neural information processing systems*, 20, 2007.
- [32] Ali Rahimi and Benjamin Recht. Uniform approximation of functions with random bases. In *2008 46th annual allerton conference on communication, control, and computing*, pages 555–561. IEEE, 2008.
- [33] Wouter F Schmidt, Martin A Kraaijveld, Robert PW Duin, et al. Feed forward neural networks with random weights. In *International conference on pattern recognition*, pages 1–1. IEEE Computer Society Press, 1992.
- [34] Claude Elwood Shannon. Communication in the presence of noise. *Proceedings of the IRE*, 37(1):10–21, 1949.
- [35] Vincent Sitzmann, Eric Chan, Richard Tucker, Noah Snaveley, and Gordon Wetzstein. Metasdf: Meta-learning signed distance functions. *Advances in Neural Information Processing Systems*, 33:10136–10147, 2020.
- [36] Vincent Sitzmann, Julien Martel, Alexander Bergman, David Lindell, and Gordon Wetzstein. Implicit neural representations with periodic activation functions. *Advances in neural information processing systems*, 33:7462–7473, 2020.
- [37] Vincent Sitzmann, Justus Thies, Felix Heide, Matthias Nießner, Gordon Wetzstein, and Michael Zollhofer. Deepvoxels: Learning persistent 3d feature embeddings. In *Proceedings of the IEEE/CVF Conference on Computer Vision and Pattern Recognition*, pages 2437–2446, 2019.
- [38] Jasper Snoek, Hugo Larochelle, and Ryan P Adams. Practical bayesian optimization of machine learning algorithms. *Advances in neural information processing systems*, 25, 2012.
- [39] Maria Luisa Taccari, He Wang, Somdatta Goswami, Mario De Florio, Jonathan Nuttall, Xiaohui Chen, and Peter K Jimack. Developing a cost-effective emulator for groundwater flow modeling using deep neural operators. *Journal of Hydrology*, 630:130551, 2024.
- [40] Matthew Tancik, Ben Mildenhall, Terrance Wang, Divi Schmidt, Pratul P Srinivasan, Jonathan T Barron, and Ren Ng. Learned initializations for optimizing coordinate-based neural representations. In *Proceedings of the IEEE/CVF Conference on Computer Vision and Pattern Recognition*, pages 2846–2855, 2021.
- [41] Matthew Tancik, Pratul Srinivasan, Ben Mildenhall, Sara Fridovich-Keil, Nithin Raghavan, Utkarsh Singhal, Ravi Ramamoorthi, Jonathan Barron, and Ren Ng. Fourier features let networks learn high frequency functions in low dimensional domains. *Advances in neural information processing systems*, 33:7537–7547, 2020.
- [42] Sifan Wang, Hanwen Wang, and Paris Perdikaris. Learning the solution operator of parametric partial differential equations with physics-informed deepnets. *Science advances*, 7(40):eabi8605, 2021.
- [43] Hassler Whitney. Differentiable manifolds. *Annals of Mathematics*, 37(3):645–680, 1936.
- [44] Hassler Whitney. The self-intersections of a smooth n -manifold in $2n$ -space. *Annals of Mathematics*, 45(2):220–246, 1944.
- [45] Norbert Wiener. The homogeneous chaos. *American Journal of Mathematics*, 60(4):897–936, 1938.
- [46] John Wright, Allen Y Yang, Arvind Ganesh, S Shankar Sastry, and Yi Ma. Robust face recognition via sparse representation. *IEEE transactions on pattern analysis and machine intelligence*, 31(2):210–227, 2008.

- [47] Yiheng Xie, Towaki Takikawa, Shunsuke Saito, Or Litany, Shiqin Yan, Numair Khan, Federico Tombari, James Tompkin, Vincent Sitzmann, and Srinath Sridhar. Neural fields in visual computing and beyond. *Computer Graphics Forum*, 41(2):641–676, 2022.
- [48] Dongbin Xiu and George Em Karniadakis. The wiener–askey polynomial chaos for stochastic differential equations. *SIAM journal on scientific computing*, 24(2):619–644, 2002.
- [49] Biao Zhang and Rico Sennrich. Root mean square layer normalization. *Advances in Neural Information Processing Systems*, 32, 2019.

Appendix

Complementary results for the numerical examples are provided in Appendices A to C. Appendix E lists the hyperparameters used for each problem. An ablation study for Algorithm 1, comparing our method with GPOD, is presented in Appendix F. Moreover, the use of random projections as an alternative for finding vector representations of input or output function data has been studied and compared to our proposed dictionary learning algorithm. Appendix G summarizes the formulation for Gaussian random field generation.

A Nonlinear 1D Darcy’s Equation

Figure 14(a) shows the reconstruction errors during the dictionary learning iterations. With a total of 10 learned basis functions, the data can be reconstructed with high accuracy, as shown by the distribution of errors in Figure 14(b) for both training and testing datasets.

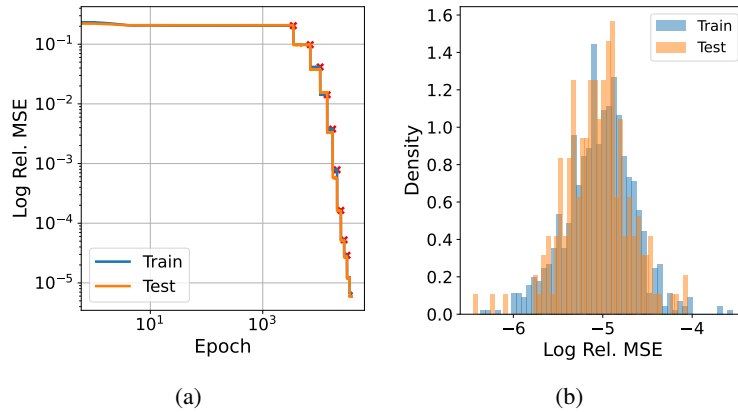


Figure 14: 1D Nonlinear Darcy Example: (a) Loss function during optimization iterations for dictionary learning of the input basis functions. (b) Distribution of reconstruction errors for the train and test datasets after training.

The history of the loss function during the operator learning stage is plotted in Figure 15(a). In Figure 15(b), the distribution of output function prediction errors after training is shown. The results suggest that the training is successful and the output function prediction via RINO is very accurate.

B Nonlinear 2D Darcy’s Equation

Figure 16(a) shows the reconstruction errors during the dictionary learning iterations. With a total of 57 learned basis functions, the data can be reconstructed with high accuracy, as shown by the distribution of errors in Figure 16(b) for both training and testing datasets. Notice that the learned dictionary allows us to represent data with 57 dimensions, which is much less than the ambient dimension of the discretized input function on a 20×20 grid. Therefore, we not only bypass the resolution dependence but also achieve a rich representation with lower dimension than the ambient data dimensionality. From a computational perspective, the input dimension for the branch network is 57, whereas using an MLP branch for the vanilla DeepONet requires 400 dimensions.

The history of the loss function during the operator learning stage is plotted in Figure 17(a). In Figure 17(b), the distribution of output function prediction errors after training is shown.

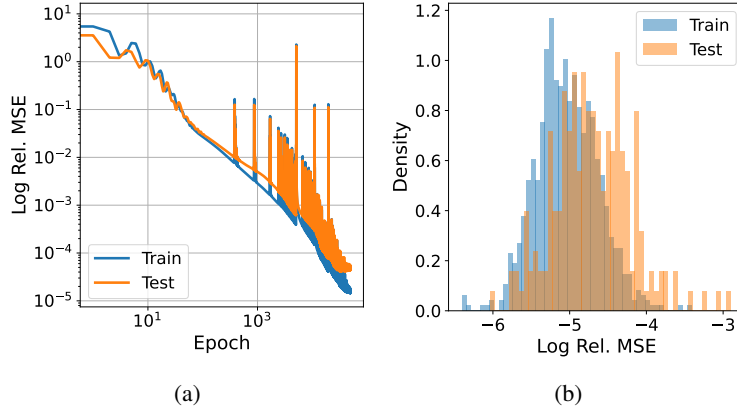


Figure 15: 1D Nonlinear Darcy Example: (a) Loss function during optimization iterations for operator learning. (b) Distribution of output function prediction errors for the training and testing datasets after training.

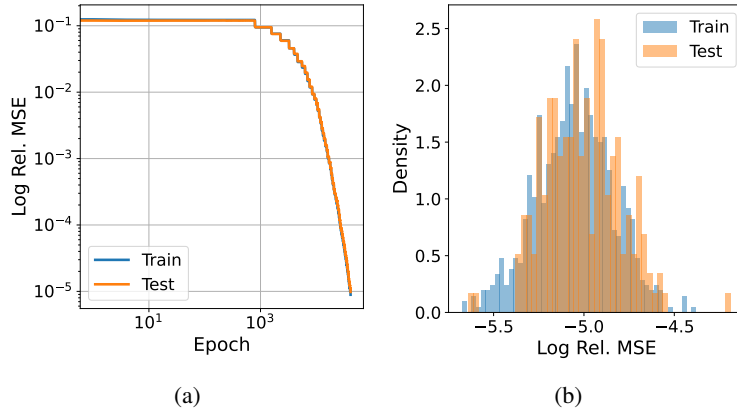


Figure 16: 2D Nonlinear Darcy Example: (a) Loss function during optimization iterations for dictionary learning of the input basis functions. (b) Distribution of reconstruction errors for the train and test datasets after training.

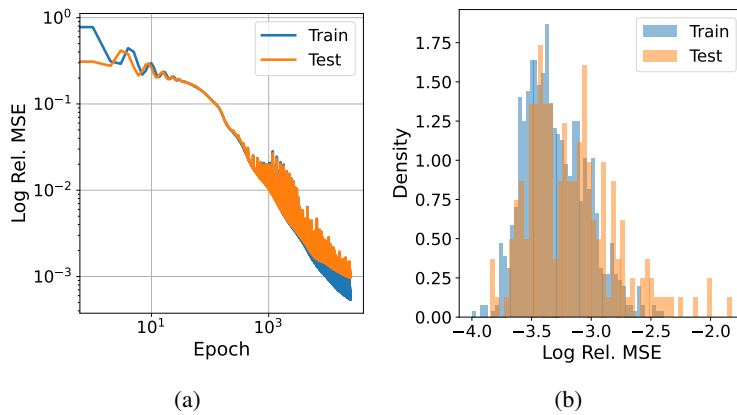


Figure 17: 2D Nonlinear Darcy Example: (a) Loss function during optimization iterations for operator learning. (b) Distribution of output function prediction errors for the training and testing datasets after training.

Two examples of the test predictions for the output field are shown in Figures 18 and 19, corresponding to the 75th percentile error and the median error, respectively. In each example, the queried point cloud input function data has different numbers of points and locations because the masked information varies among them.

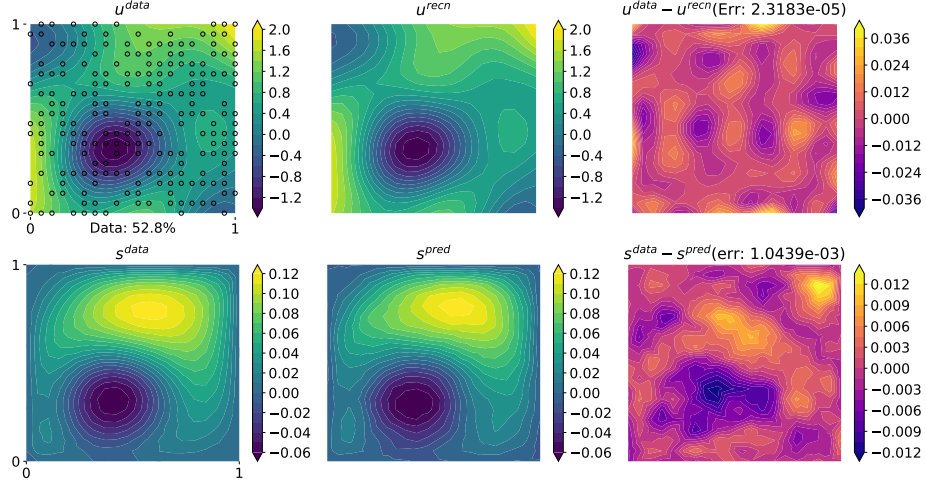


Figure 18: 2D Nonlinear Darcy Example: The case with 75th percentile output function prediction error. The top left figure shows the queried input function data $u(\boldsymbol{x})$, with black circle symbols indicating the queried data. The middle top figure shows the input field reconstruction via the learned dictionary. The top right figure shows the error between the reconstructed input field and the ground truth. The bottom figures show the output field $s(\boldsymbol{y})$, the RINO prediction, and its corresponding errors.

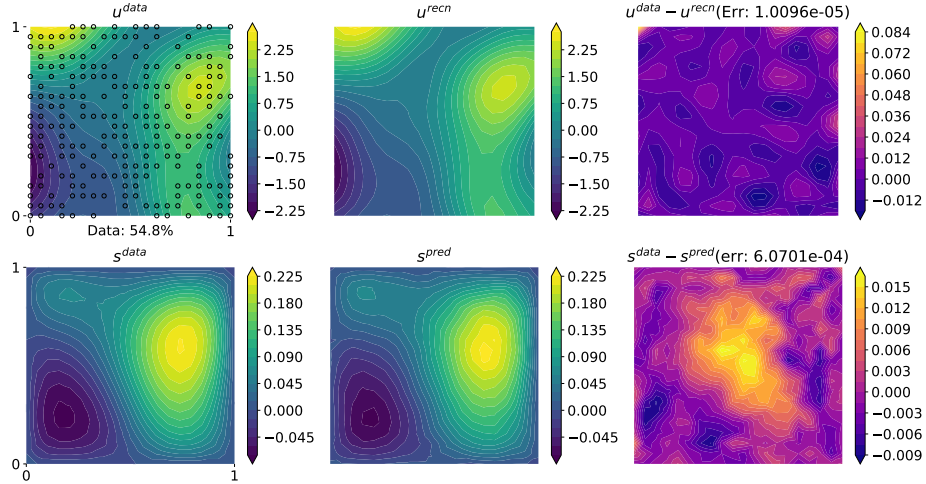


Figure 19: 2D Nonlinear Darcy Example: The case with 50th percentile output function prediction error. The top left figure shows the queried input function data $u(\boldsymbol{x})$, with black circle symbols indicating the queried data. The middle top figure shows the input field reconstruction via the learned dictionary. The top right figure shows the error between the reconstructed input field and the ground truth. The bottom figures show the output field $s(\boldsymbol{y})$, the RINO prediction, and its corresponding errors.

C Burgers' Equation

Figure 20(a) shows the reconstruction errors during the dictionary learning iterations. The distribution of reconstruction errors in Figure 20(b) for both training and testing datasets indicates that the learned dictionary, with a total of 16 basis functions, can satisfactorily represent the input function data.

Figure 21(a) illustrates the evolution of the loss function during the operator learning stage. The distribution of output function prediction errors after training is depicted in Figure 21(b). These results indicate that the training was successful, leading to accurate output function predictions by RINO.

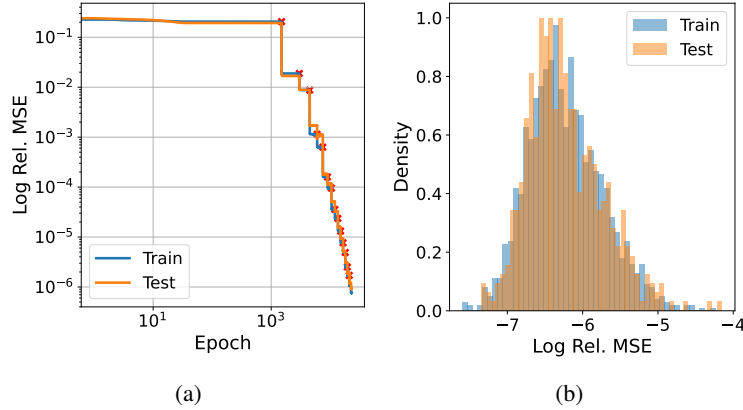


Figure 20: Burgers' Equation: (a) Loss function during optimization iterations for dictionary learning of the input basis functions. (b) Distribution of reconstruction errors for the train and test datasets after training.

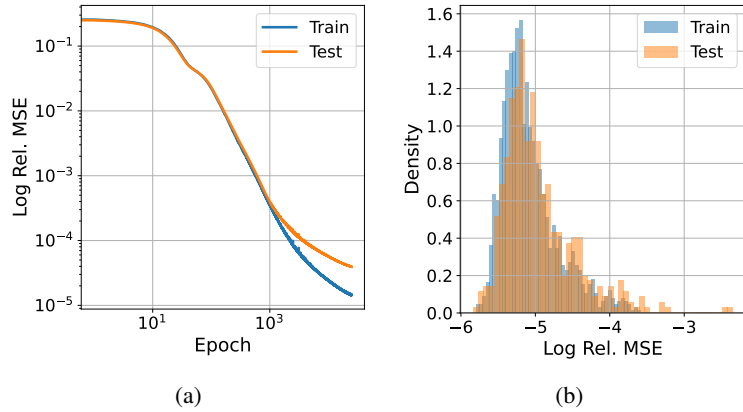


Figure 21: Burgers' Equation: (a) Loss function during optimization iterations for operator learning. (b) Distribution of output function prediction errors for the training and testing datasets after training.

D Nonlinear 2D Darcy's Equation on Unstructured Meshes

Figure 22(a) shows the reconstruction errors during the dictionary learning iterations for the input function point cloud data. The distribution of reconstruction errors in Figure 22(b) suggests that a satisfactory reconstruction error can be achieved by the learned dictionary with 40 basis functions.

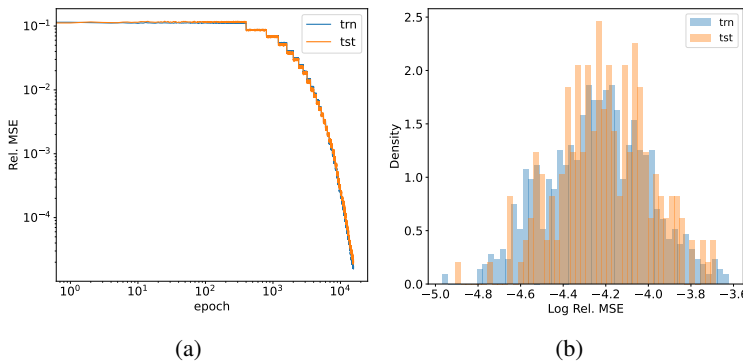


Figure 22: 2D Darcy's Equation on Unstructured Meshes: (a) Loss function during optimization iterations for dictionary learning of the input basis functions. (b) Distribution of reconstruction errors for the train and test datasets after training.

The evolution of the loss function during the operator learning stage is depicted in Figure 23(a) where both branch and trunk nets are unknown *a priori*. The distribution of output function prediction errors after training is plotted in Figure 23(b). A successful training with satisfactory accuracy in RINO predictions is confirmed by the results.

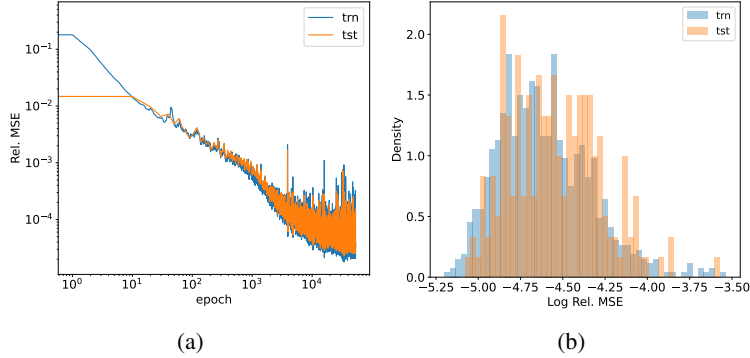


Figure 23: 2D Darcy’s Equation on Unstructured Meshes: (a) Loss function during optimization iterations for operator learning. (b) Distribution of output function prediction errors for the training and testing datasets after training.

As discussed in the main text, the proposed method can flexibly use a predefined trunk network by substituting a learned dictionary of appropriate basis functions for the output function data. Figure 24 shows the reconstruction error distributions for the output function point cloud data, where Algorithm 2 was able to identify an appropriate dictionary of 54 basis functions that span the output solution fields.

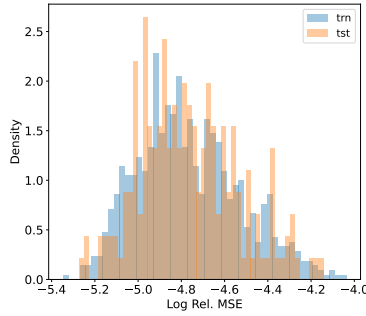


Figure 24: 2D Darcy’s Equation on Unstructured Meshes: Distribution of reconstruction errors for the training and test datasets after learning the dictionary of basis functions for the output function.

The evolution of the loss function during the operator learning stage for the case where we utilized the learned, predefined trunk dictionary is depicted in Figure 25(a), where only the branch network is trained. The distribution of output function prediction errors after training is plotted in Figure 25(b). A successful training with satisfactory accuracy is confirmed by the results for the case where we indirectly learned a mapping between the coefficients of two sets of weakly orthogonal basis functions: one corresponding to the input function data and the other to the output function data, which were identified separately and *offline*.

E Network Architecture

In this work, the neural network architectures and hyperparameters were chosen through manual trial and error and, therefore, are not optimized. As a result, the performance may improve by utilizing rigorous hyperparameter optimization methods, such as Bayesian optimization [38].

The hyperparameters utilized for learning the dictionary are listed in Table 2. The column “2D Darcy*” corresponds to the last numerical example, where we solve the nonlinear 2D Darcy problem on different finite element meshes from one realization to another.

The same learning rate of 0.001 is chosen for the operator learning task. The input data to the branch and trunk networks are not normalized in all cases except for the nonlinear 2D Darcy’s equation, where the sparse codes obtained from the dictionary are linearly normalized to have a minimum of 0 and a maximum of 1 before training.

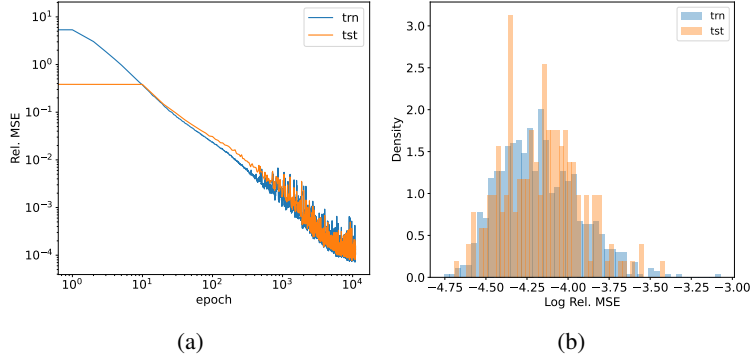


Figure 25: 2D Darcy’s Equation on Unstructured Meshes: (a) Loss function during optimization iterations for operator learning with the predefined dictionary learned trunk net. (b) Distribution of output function prediction errors for the training and testing datasets after training.

Table 2: Hyperparameters for the dictionary learning algorithm where SIRENs are used as basis functions.

	Antiderivative	1D Darcy	2D Darcy	Burger’s	2D Darcy*
Number of hidden units	20	30	50	30	20
Number of hidden layers	2	2	3	2	2
Learning rate	1.66×10^{-4}	3×10^{-4}	6.6×10^{-4}	6.6×10^{-4}	4×10^{-4}
λ	10^{-4}	10^{-4}	10^{-5}	10^{-5}	10^{-3}
ω_0	5	10	10	10	10

In the case of the antiderivative, no branch network is utilized; the sparse codes obtained from the dictionary are directly considered as coefficients for the trunk basis, making the branch network essentially an identity operator. The architecture of the hidden layers in the branch networks for other examples are as follows:

- Nonlinear 1D Darcy: MLP [50 | ReLU | 50]
- Nonlinear 2D Darcy: MLP [50 | ReLU | 100]
- Burgers’ equation: MLP [100 | Tanh | 100 | Tanh | 70]
- Nonlinear 2D Darcy*: MLP [100 | Tanh | 100]

The architecture of the hidden layers in the trunk network are:

- Antiderivative: SIREN [50, 50] with $w_0 = 5$
- Nonlinear 1D Darcy: SIREN [50, 50, 50] with $w_0 = 5$
- Nonlinear 2D Darcy: MLP [50 | ReLU | 50 | ReLU | 100]
- Nonlinear 2D Darcy*: SIREN [100, 100, 100] with $w_0 = 10$

For the “nonlinear 2D Darcy*” case, we also compare it with the scenario where our dictionary learning algorithm is applied to output function realizations to learn output basis functions *offline* and use them as a predefined trunk net. In this setup, each output basis was parametrized by SIREN [20 | 20] with $w_0 = 10$. The sparsity parameter $\lambda = 10^{-4}$ and the learning rate is 10^{-3} .

F Ablation Study: Comparison with Gappy Proper Orthogonal Decomposition and Random Projection

In this example, we aim to empirically demonstrate that Algorithm 1 can effectively identify (weakly) orthogonal basis functions that accurately represent point clouds sampled from a random function. To enable a comparison with the GPOD method, we configure the problem setup to be compatible with it. Our method shares similarities with GPOD

but offers greater flexibility: it can operate with point cloud data instead of regular grids and, more importantly, it finds continuous, fully differentiable basis functions rather than finite-dimensional basis vectors. Moreover, with GPOD, one cannot query an arbitrary sensor location that differs from the union of sensor locations used in the training data due to its discrete nature, while our approach allows queries at any location.

We purposely generate several realizations of random functions $u(x)$ that are inherently correlated by sharing a common low-dimensional structure. The i -th realization is given by:

$$u^{(i)}(x) = \sum_{l=1}^3 \alpha_l^{(i)} \psi_l(x), \quad x \in [0, 1], \quad (24)$$

where the coefficients are assumed to be normally distributed, $\alpha_l^{(i)} \sim \mathcal{N}(0, 1)$, and the basis functions are the 6th-order Legendre polynomial, $\psi_1(x) = P_6(x)$; the cosine function, $\psi_2(x) = \cos(3.3\pi x)$; and the absolute value function, $\psi_3(x) = 2|x| - 1$, as depicted in Figure 26(a). The random functions are generated similarly to PCE, where deterministic functions with random coefficients are used to model stochastic processes. Clearly, such random functions can be fully characterized by at most three modes, each corresponding to one of these functions. 200 realizations of this random function, where each realization is discretized at 100 uniform sensor locations, establish our “complete” training dataset, as plotted in a matrix format in Figure 26(b). In this figure, each row represents a realization, each column corresponds to a sensor location, and the colors at the (i, j) location indicate the value of the i -th realization at the j -th sensor location. The “gappy” version of the data is created by randomly masking $R\%$ of each realization. For example, in Figure 26(c), the mask matrix for masking 90% of the information is presented.

Note that the basis functions used in the generative function, Eq. (24), are purposely chosen to not be orthogonal (see Figure 28(a)) and exhibit a multiscale nature, as they have different length scales. It may be of interest to investigate whether our algorithm can find orthogonal basis functions, how similar these basis functions are to those found by GPOD, and how closely they resemble the non-orthogonal basis functions used for generating the data. It is known that the basis functions learned by PCA-based algorithms, such as GPOD, will be orthogonal.

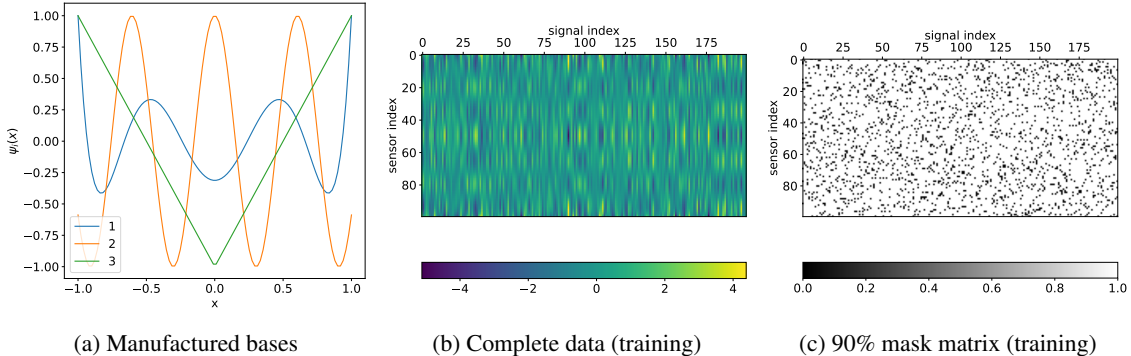


Figure 26: (a) Basis functions used to generate random functions. (b) Complete training data set generated from 200 such functions, each sampled at 100 sensor locations. (c) Example of the mask matrix representing 90% masked training data for each function, where white (value 1) indicates masked entries.

In Figure 27, we have plotted the discovered bases from GPOD and those discovered by our method at various levels of masked data, ranging from 50% to 95%. With sufficient unmasked data (e.g., $R = 50\%$, 75%), the first two modes (orange and blue curves) from both GPOD and our algorithm closely resemble the cosine function and the Legendre function, which were initially weakly orthogonal in the generative process, as shown in Figure 28(a). However, the third mode (green curve) differs from the absolute value function, which was the non-orthogonal basis in the generative process, see Figure 28(a). From the GPOD perspective, this is expected since it represents data using orthogonal bases. Interestingly, the third basis function in our method exhibits almost the same behavior as the third basis in GPOD. Furthermore, the order of the bases in our approach matches the order in GPOD. These similarities occur even though we only weakly enforce the orthogonality constraint and do not enforce ordering based on data variance, as is the case with GPOD. The (weak) orthogonality of the bases in our method can be confirmed by the inner product calculation shown in Figure 28(c).

Up to a certain level, GPOD results are consistent and can achieve almost zero reconstruction error. However, at higher levels of masking (e.g., $R = 90\%$), its accuracy drops significantly. Our method, on the other hand, can still operate with reduced accuracy under similar conditions. We hypothesize that this is due to our method’s inductive bias towards

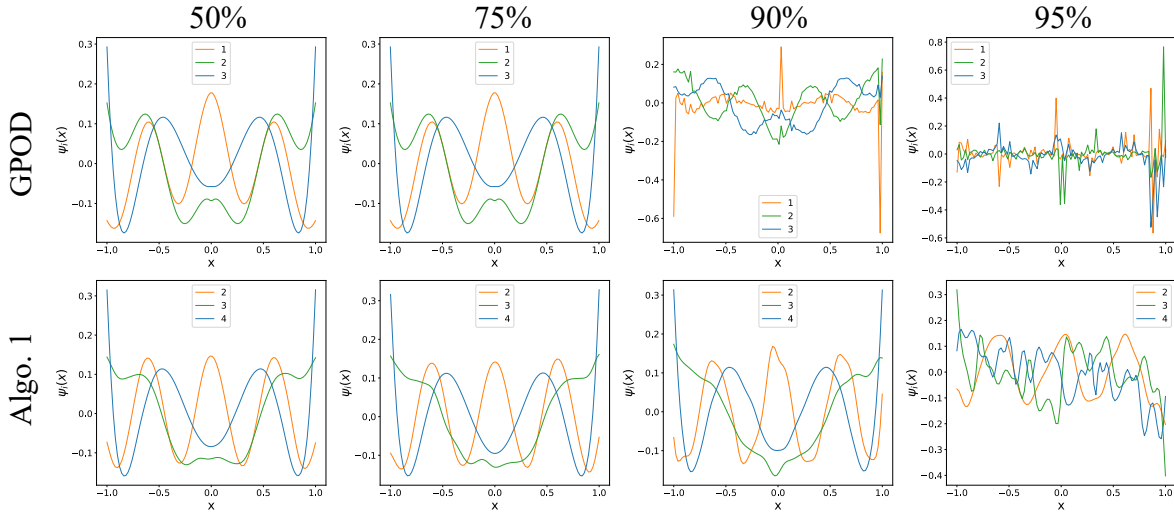


Figure 27: Comparison of identified bases using Gappy POD and Algorithm 1 at different levels of masked data. The percentage indicates the extent of data masking.

smoothness in the basis functions, as they are parameterized by SIREN, whereas GPOD does not incorporate such an assumption. Nonetheless, our method also becomes less effective when the data is extremely sparse, as evidenced by the case with $R = 95\%$.

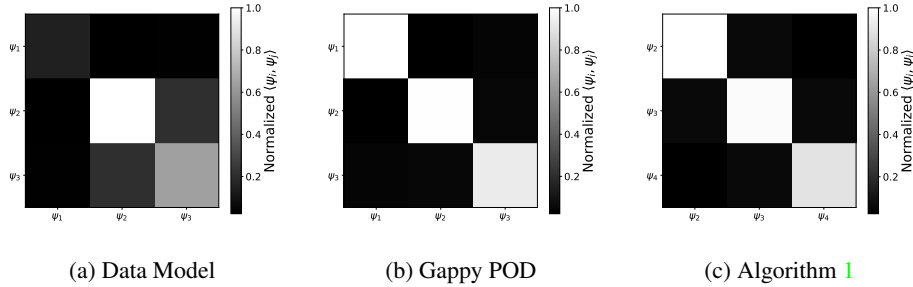


Figure 28: Orthogonality check among basis functions: (a) Basis functions used to generate random function data (see Eq. 24). (b) Basis vectors identified by the Gappy POD algorithm, and (c) basis functions identified by the proposed algorithm with 50% of the data masked.

The reconstruction errors at various level of masking percentages are listed in Table 3. The GPOD is a deterministic algorithm and, hence, there is no randomness regarding its prediction accuracy. However, our method relies on INRs as basis functions, where different randomly initialized parameters for the neural network may result in different predictions. Therefore, we conducted the training five times, each with different initial neural network parameters. As the results suggest, the accuracy of GPOD in this problem is better than Algorithm 1 and is resilient to the amount of masked data up to a certain limit, after which it suddenly fails catastrophically. On the other hand, our scheme gradually reduces accuracy with respect to the amount of masked data and remains performant under conditions where GPOD fails. This abrupt reduction in accuracy might be undesirable, particularly for data acquisition tasks where a well-behaved continuous error feedback is important.

In Figure 29, we demonstrate the generalization ability of the proposed method. The shaded regions in green and purple represent two types of generalization: in-sample and out-of-sample in-distribution. If one attempts per-sample curve fitting, there is no guarantee that such fitting will capture the underlying ground truth, as fluctuations in these regions exceed the data frequency for interpolation; according to the Nyquist sampling theorem, the sampling rate should be at least twice the frequency of changes. Particularly under this scenario, the purple region can be considered pure extrapolation, which is known to be challenging without additional assumptions. The reason our reconstruction

	$R\%$	Test Error (mean \pm std)	Train Error
GPOD			
	25	$3.601e-08 \pm 0$	$1.407e-08 \pm 0$
	50	$4.253e-08 \pm 0$	$2.670e-08 \pm 0$
	75	$2.360e-08 \pm 0$	$2.360e-08 \pm 0$
	90	$2.474e+01 \pm 0$	$2.390e+02 \pm 0$
	95	$3.991e-02 \pm 0$	$2.357e+03 \pm 0$
Algorithm 1			
	25	$3.914e-05 \pm 3.403e-06$	$3.733e-05 \pm 3.273e-06$
	50	$9.678e-05 \pm 1.012e-05$	$9.291e-05 \pm 9.549e-06$
	75	$6.502e-04 \pm 4.340e-05$	$6.263e-04 \pm 4.066e-05$
	90	$3.302e-03 \pm 2.357e-04$	$2.609e-03 \pm 1.358e-04$
	95	$8.262e+02 \pm 3.489e-03$	$1.423e-02 \pm 2.625e-03$

Table 3: Reconstruction errors for various randomly masked data. The same masking percentage R is used for both training and testing.

method performs so well is that it identifies common structures by considering **all samples (realizations)**, not just individual samples, and utilizes basis functions that harness this structure. Moreover, although the available data in these samples are highly asymmetric, the reconstruction is almost symmetric. This symmetry is due to the identified symmetric basis functions, which are one of the main characteristics of the generated data, as the generative basis functions are symmetric. This property cannot be achieved through per-sample curve fitting. Therefore, we do not advocate for methods that attempt per-sample curve fitting and then align the samples by interpolation at fixed sensor locations.

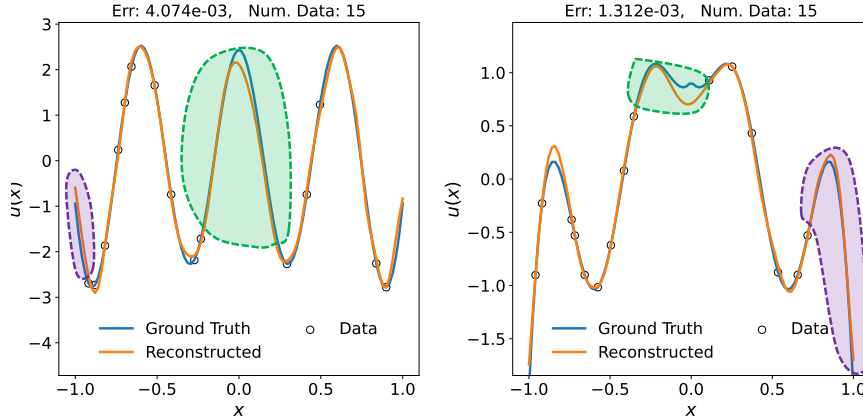


Figure 29: Reconstruction generalization capability of the proposed dictionary learning method, demonstrated on two queried samples, with the dictionary trained on only 15% of the data.

One may consider using random smooth functions, such as those parameterized by a shallow neural network [33, 31, 32, 16], as a method to construct basis functions in a predefined manner. These functions can naturally impose smoothness as inductive biases and can remain resolution-independent during the reconstruction and projection steps. Here we aim to benchmark and compare their performance using this pedagogical example. To this end, we consider two cases: 1) random shallow ReLU networks, where each basis is a ReLU network with 20 hidden neurons randomly initialized, and 2) classical cosine basis functions with random frequency and phase shifts as follows:

$$\psi_i(x) = \cos(w_i x + b_i); w_i \sim \mathcal{N}(0, \sigma = 2\pi), b_i \sim \text{Uniform}[0, 2\pi], \quad (25)$$

for the i -th cosine basis functions. For completeness, we also consider the classical monomial and Legendre basis functions (deterministic). In Figure 30, we compare the reconstruction performance of these sets of basis functions by increasing the number of basis functions used in each set and by gradually sparsifying the data.

When the data density is sufficiently high, as shown in Figure 30(a), random ReLU, random cosine, and Legendre bases deliver satisfactory performance. However, in our numerical experiments, they appear to require two orders

of magnitude more basis functions than ours, which is not ideal for downstream learning tasks, as one would prefer to operate with an embedding space of dimension 3 rather than 100. This preference is due to both computational efficiency and the fact that the amount of data required for such learning tasks may scale exponentially with respect to dimensionality. As data sparsity increases, as shown in Figure 30(b and c), the performance gap between our method and others grows more pronounced. For instance, with 85% of the data masked in Figure 30(c), the performance of the other methods becomes unacceptable. This decline is due to the limited data, making these other methods more prone to overfitting.

In all cases, monomial basis functions did not perform well, regardless of the number of chosen basis elements or the amount of data available. This may be due to the fact that monomial bases of type $\psi_n(x) = x^n$ lack the appropriate inductive biases needed to effectively learn the data, particularly when the data exhibits sinusoidal behavior. This observation underscores the importance of selecting a sufficiently flexible set of basis functions, which is often not obvious at first. Therefore, an approach that can automatically identify the right set of bases in a data-driven manner is crucial, and this is one of the key contributions of this paper.

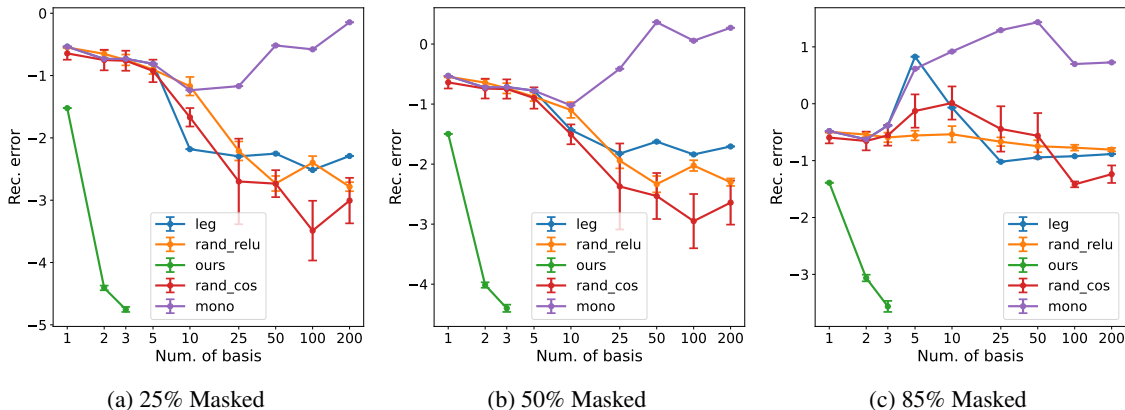


Figure 30: Comparison of reconstruction accuracy on test data using four distinct sets of basis functions. Each set is evaluated through five independent computations, with randomly chosen parameters for stochastic methods; for deterministic basis functions (monomial and Legendre), no randomness is involved. As the results demonstrate, even as data sparsity increases, our method consistently outperforms alternatives. Notably, our approach achieves this with significantly fewer basis functions, utilizing only 3 compared to 100 in other methods.

To further analyze the performance of random bases in the case where the data has the highest sparsity (i.e., 85% masked data), we plotted the reconstruction curves for the worst case and the 25th quintile in terms of relative errors in Figure 31. As expected (and as consistent with the literature [31, 16]), the random basis functions perform well in the interpolation regime but poorly in the extrapolation regime beyond the data support (as observed in the purple-shaded areas in these figures). Moreover, the underlying generative process of the data is symmetric at $x = 0$, see Figure 26(a). However, there is no guarantee that this symmetry can be recovered using random basis functions. As already discussed, these issues do not arise with our method, as we learn appropriate basis functions by considering the common correlation structure across all realizations, rather than merely interpolating for each individual realization.

Spanning versus Parametrization As we have shown, **linear** (with respect to the basis functions) projection and reconstruction using linearly independent random basis functions often requires exponentially more basis functions compared to an optimal orthogonal basis set, provided the signals of interest can be spanned by such an optimal orthogonal basis. Although this is aligned with the linear theory [16], it does not take advantage of an additional possibility, consistent with established embedding theorems, which suggests that one can *embed* an n -dimensional manifold with at most $2n + 1$ generic observables [43, 44] (in our case, the components of our data in $2n + 1$ random basis functions). These projections do not *span* our intrinsically n -dimensional data; yet, the projections of the data in any additional random basis functions can be obtained as *functions* of the first $2n + 1$ ones. We say that the $2n + 1$ basis functions *parametrize* the data, but do not *span* them. The approximation of the data can now be achieved via nonlinear parameterization, which maps the projected solution on the hyperplane back to the target manifold. This approach shares similarities with the post-processing Galerkin method [20, 14]. However, such nonlinear parameterization may have some caveats: (1) it is less interpretable than our proposed spanning scheme; (2) the number of basis functions is not known *a priori*—only an upper bound is provided—while our approach adaptively identifies the number of basis functions according to a tolerance; (3) The embedding space constructed via random projection is highly sensitive to sampling, which undermines the uniqueness of the signal representation. To elaborate further on the last point, we

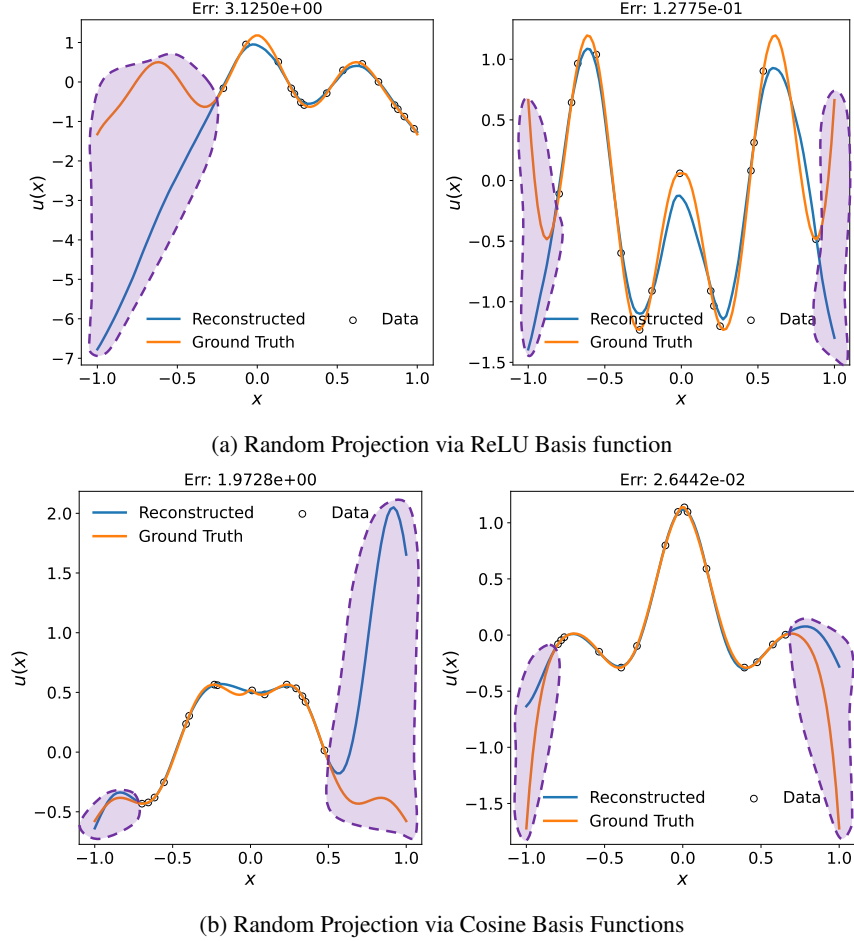


Figure 31: Reconstruction curves for the worst case and the 25th quantile in terms of relative reconstruction error in the case where 85% of the data was masked.

conducted a simple test as follows. We pick one of the signal realization from the test data set and aim to reconstruct the signal with three linearly independent random cosine basis, as mentioned earlier. To assess the sensitivity of the embeddings, we consider five cases where half of the points are masked in each case. However, the locations of these masked points are randomly selected and vary from one case to another. The embeddings obtained from random projection, shown in the right column of Figure 32(a), are clearly dependent on the location of the samples. The left column shows the reconstructed signal, where we again observe high variance. In contrast, the projection via optimal orthogonal basis functions, as shown in Figure 32(b), is consistent across cases and independent of the sample locations.

G Random Field Generation

Similar to the strategy utilized in [22, 42], the random but correlated input functions $u(\mathbf{x})$ for data generation are sampled from a Gaussian random process $u(\mathbf{x}) \sim \mathcal{GP}(0, \text{Cov}(\mathbf{x}_1, \mathbf{x}_2; l))$ with zero mean and a covariance function defined the radial basis function (RBF) with an isotropic kernel as follows:

$$\text{Cov}(\mathbf{x}_1, \mathbf{x}_2; l) = \exp\left(-\frac{\|\mathbf{x}_1 - \mathbf{x}_2\|_{\mathcal{X}}^2}{2l^2}\right), \quad (26)$$

where $\mathbf{x}_1, \mathbf{x}_2 \in \mathcal{X}$ and $\|\mathbf{x}_1 - \mathbf{x}_2\|_{\mathcal{X}}$ induces a norm associated with the domain \mathcal{X} . Here, in the 1D and 2D cases, the chosen norm is the L_2 -norm.

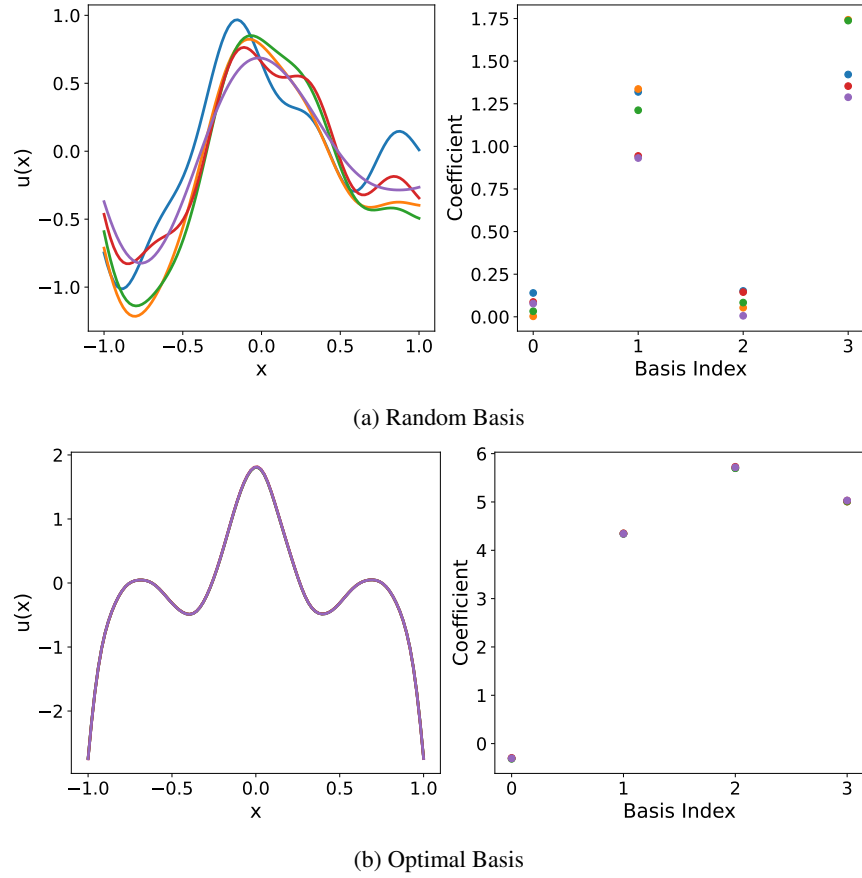


Figure 32: Consistency check of the embeddings obtained from projections via (a) random basis and (b) optimal basis sets. The right column display the coefficients corresponding to each basis function, while the left column show the reconstructed full fields based on the identified coefficients. Different colors represent distinct queried datasets, where the number of data points remains the same but their locations are chosen randomly and differ from one dataset to another.